



Universidad de Sonora

Postgrado en Nanotecnología
Departamento de Física

Electron dispersion and bound states in
the vicinity of nanostructures

by

Alejandro Castellanos-Jaramillo

Dissertation submitted in fulfillment of the requirements
of the degree of Doctor in Nanotechnology.

Universidad de Sonora

Repositorio Institucional UNISON



**"El saber de mis hijos
hará mi grandeza"**



Excepto si se señala otra cosa, la licencia del ítem se describe como openAccess

VOTOS APROBATORIOS

DR. MARIO ENRIQUE ÁLVAREZ RAMOS Coordinador de Posgrado en Nanotecnología

Por medio de la presente, nos permitimos informarle que los miembros del Jurado designado para revisar la Tesis de Doctorado intitulada:

"Electron dispersion and bound states in the vicinity of nanostructures.",

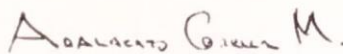
presentada por:

Alejandro Castellanos Jaramillo

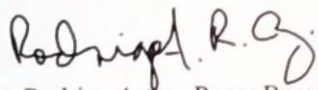
Hemos revisado y dado su VOTO APROBATORIO ya que cumple con los requisitos para la obtención del Título de Grado de Doctor en Nanotecnología:



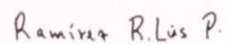
Dr. Arnulfo Castellanos Moreno



Dr. Adalberto Corella Madueño



Dr. Rodrigo Arturo Rosas Burgos



Dr. Luis Patricio Ramirez Rodriguez



Dr. Francisco Adrián Duarte Alcaraz
(EXTERNO)

Papers published for this dissertation

Alejandro Castellanos-Jaramillo, Arnulfo Castellanos-Moreno , Eur. J. Phys. 39 (2018) 065403 (18pp) <https://doi.org/10.1088/1361-6404/aadcd7>

Alejandro Castellanos-Jaramillo, Arnulfo Castellanos-Moreno , J Nanopart Res (2019) 21:141, <https://doi.org/10.1007/s11051-019-4586-2>

Alejandro Castellanos-Jaramillo, Arnulfo Castellanos-Moreno, J Nanopart Res (2020) 22:149, <https://doi.org/10.1007/s11051-020-04889->

Alejandro Castellanos-Jaramillo, Sergio Gutiérrez-López, Arnulfo Castellanos-Moreno, Journal of Nanoparticle Research (2020) 22:210, <https://doi.org/10.1007/s11051-020-04936-1>

Electron dispersion and bound states in the vicinity of nanostructures.

Alejandro Castellanos Jaramillo.

Advisor: Arnulfo Castellanos Moreno

Co-advisor: Rodrigo Arturo Rosas Burgos.

Universidad de Sonora, Departamento de Física, Posgrado en Nanotecnología

CONTENTS

General Introduction	7
1 Spatial and temporal description of electron diffraction through a double-slit at the nanometre scale	10
1.1 Introduction	11
1.2 Nondimensionalization, the FDTD method, and stability	12
1.2.1 Nondimensionalization and scale selection	12
1.2.2 The FDTD method	13
1.2.3 Stability conditions	15
1.3 Physical System	16
1.4 Numerical Results	18
1.4.1 Configuration Space	18
1.4.2 Collection at fixed points through time and comparison of local information	22
1.4.3 Momentum space	24
1.5 Conclusions	26
1.5.1 Conceptual exercise	26
1.5.2 About the computer program	27
2 Bidimensional Bound States for Charged Polar Nanoparticles	28
2.1 Introduction	29
2.2 Physical system	30
2.3 Non-dimensionalized equation	31
2.4 Separation of variables	32
2.5 Matthieu equation and its solutions	34
2.6 Radial equation	37
2.7 Transition rates (A-coefficients)	39
2.8 Conclusions	40
3 Behavior of an electron in the vicinity of a tridimensional charged polar nanoparticle through a classical and quantum constant of motion	41
3.1 Introduction	42
3.2 Classical approach	42
3.2.1 Calculation of the constant of motion from the Hamilton-Jacobi equation.	43

3.2.2	Calculating the constant of motion from a Newtonian approach	45
3.2.3	Analysis of motion in the radial coordinate	46
3.2.4	Analysis of motion of the angular coordinate	47
3.3	Quantum approach	47
3.3.1	Non-dimensionalized equation	48
3.3.2	Separation of variables	49
3.3.3	Angular equation	51
3.3.4	Solution to the matrix equation	53
3.3.5	Plots	53
3.4	Radial equation	54
3.4.1	Ionization energies of the system	58
3.5	Conclusions	59

LIST OF FIGURES

1.1	Spatial representation of the potential barrier, $f(\vec{x})$	13
1.2	Visualization of the temporal discretization scheme. The real and imaginary components are shifted in time by $\frac{1}{2}\Delta t$. The updating of ψ_1 depends on ψ_2 and viceversa. a) Update diagram of ψ_1 using (1.14), b) Update diagram of ψ_2 using (1.15).	15
1.3	Spatial arrangement of the numerical space. The width of the box is 551 nm and its height 654 nm. Using $\tau = 1.7276 \times 10^{-14}$ s. The double-slit wall is located 215 nm from the origin, and the collector line is placed 165 nm from the wall. The wave packet travels from the lower part in the vertical direction. The vertical width of the wall is $h = 10$ nm. The width of each slit is 20 nm.	18
1.4	Shape of the wave packet before diffraction. Left: $ \psi(\vec{x}, T = 165) ^2$, $T = 165$, which is equivalent to $t = 0.356$ ps. Right: wave packet at $T = 700$, which is equivalent to $t = 1.51$ ps. The wave packet undergoes gradual dispersion over time.	19
1.5	Appearance of interference pattern in the probability density, the potential is situated at $y = 0$. Left: at $T = 1020$, which corresponds to $t = 2.203$ ps. It forms two peaks as it passes through the double slit. Right: at $T = 1255$, which corresponds to 2.710 ps, where the beginning stages of the interference pattern appear.	19
1.6	Formation of the interference pattern in $ \psi(\vec{x}, T) ^2$, the potential is situated at $y = 0$. Left: pattern at $T = 1495$, which correspond to $t = 3.228$ ps. Right: pattern at $T = 1605$, which correspond to $t = 3.466$ ps.	20
1.7	Intersection of $ \psi(\vec{x}, T) ^2$ with a plane parallel to the double slit, where the position of the potential wall is at $y = 0$. This depiction is analogous to electron intensities hitting a screen.	20
1.8	Intersection curves of $ \psi(\vec{x}, T) ^2$ with a plane parallel to the wall, placed at $y = 380$ nm. The times are: $T = \{1255, 1459, 1900, 2000\}$, which in real time correspond to $t = \{2.71, 3.15, 4.10, 4.32\}$ ps. Probability currents are discernible in the in the horizontal axis.	21
1.9	Data as recorded by the collectors. It shows how the probability density increases and then diminishes over time, as the wave packet passes through them. The collectors are placed at $x = 276$ nm, $k = 0, 1, \dots, 13$; located over a line placed 65 nm ahead of the wall.	22
1.10	Depiction of the maxima $ \psi(\vec{x}_k, T) _{max}^2$, as recorded by the collectors in configuration space. It follows an interference pattern.	23

1.11	Maxima of the at fixed points in momentum space of the probability density $ \phi(\vec{x}_j, \omega) _{max}^2$. It also follows an interference pattern.	23
1.12	Left: depiction of the magnitude of the square of the absolute value of the Fourier transform $ \phi(\vec{x}_j, \omega) ^2$ with respect to ω . It takes its more significant values at lower frequencies. Right: local peaks appear for higher energies but they are practically irrelevant.	24
1.13	Depiction of the probability density $ \phi(\vec{k}, \omega) ^2$ in momentum space. Left: for $T = 1255$, which corresponds to $t = 7.71$ ps. Right: for $T = 1605$, which corresponds to 3.47 ps. There is no apparent change from one time to the next.	24
1.14	Depiction of the probability density $ \phi(k_x, k_y, t_j) ^2$ in momentum space as would be seen on perpendicular planes intersecting at $k_y = 130, 140, 160$. The curves are plotted against two distinct times t_j . As far as the precision of the numerical method allows, no changes occurred.	25
1.15	Depiction of the probability density $ \phi(k_x, k_y, t_j) ^2$ in momentum space on perpendicular planes intersecting at $k_y = 140, 160$ at two distinct times t_j . Now changes are easily discernible, with the momenta changing drastically from one time to the next.	25
2.1	λ values for different characteristic exponents ν . There is a discontinuity close to $\nu = 1.0$. In order to obtain angular functions of period π , ν must be an integer.	35
2.2	Angular functions for the first four characteristic exponents.	36
2.3	Probability amplitude. The values of ν and λ are given in table 2.1.	36
2.4	Potential for distinct values of λ . An eigenvalue for the constant of motion acts like the angular momentum, as is seen in the case when the electric dipole moment is zero.	37
2.5	Radial component of the probability amplitude for the ground state and three excited states. The quantum numbers $n = 0, 1, 2, 3$, equals the number of nodes.	38
3.1	Angular probability densities for $(GaAs)_3$, $p = 0.2589$. The values of λ are small modifications of $l(l+1)$, with $l = 0, 1, 2, 3$. The curves are slightly larger for $\theta \sim 0$	54
3.2	Angular probability densities for $(GaAs)_3$, RbC_{60} , and LiC_{60} . When p grows larger, there is a shift in probability towards the lower values of θ	55
3.3	Radial probability amplitude for the case when $p = 1$, $\lambda = 2.05822$, $m = 0$, $n = 0, 1, 2$ nodes. The third excited state presents a high probability near 2.6 nm.	56
3.4	Radial probability amplitudes. Case for when $p = 5$, ${}^5\lambda_0^1 = 2.59682$, $m = 0$, $n = 0, 1, 2$ nodes. The energy levels increase slightly and probabilities shift towards the right.	56
3.5	A) Radial probability amplitudes for their respective λ with $p = 1$ and $p = 5$. When the values of λ are closer, the curves are barely distinguishable; when it increases, the maximum value of the function decreases and shifts towards the right. B) Enlarging the picture shows the closeness of the curves for similar values of λ	57

LIST OF TABLES

2.1	Eigenvalues λ for every characteristic exponent. They must be non-negative so that the centrifugal potential responds in a manner that is similar to when the dipole is zero.	35
2.2	Energies of the ground state and for the first three bound states, where m enumerates the eigenvalue λ . For each of these, there is a potential and, in return, a set of radial solutions with its respective energy.	39
2.3	The measured Einstein coefficients with the most significant magnitude. All frequencies are located in the infrared spectrum.	39
3.1	Eigenvalues λ for $m = 0$, $m = 1$. Electric dipole moments from $p = 1$ to $p = 5$. Comparison with the values $l(l + 1)$. Changes grow with p	53
3.2	Energies for $p = 1$ and $p = 5$. When the eigenvalue λ grows, the energies increase.	57
3.3	The electron in any of these energies can absorb infrared radiation to be expelled.	58

General Introduction

The controlled manufacture of nanometric scale structures poses important challenges to the theoretical description of the physical phenomena involved. Comprehending them facilitates the design of new technologies based in manipulating matter at the atomic or molecular levels, in order to develop applications relevant to industrial processes.

This thesis addresses two concrete problems, one in the realm of electron dispersion, and another being the existence of electrons bound to a nanostructure as a whole instead of, as usual, being bound to one of the atoms.

In this work, specific emphasis is placed on the problem of electron dispersion, where novel aspects of modeling the phenomenon at nanometric scale are taken into account: 1.- The motion of electromagnetic waves in reduced spaces so minuscule that their dimensions are smaller than the length of the wave through which they propagate. These are called "sub-wavelength electromagnetic phenomena."

2.- The motion of electron packets in spaces that are too close together: the emission source, obstacles that get in their way, and the region where the phenomenon of dispersion is detected.

For the case of the motion of electrons in minuscule spaces, two problems are outlined: A) the algebraic difficulty in treating the phenomenon of dispersed outgoing waves analytically, which is complex given that nanometric scales do not allow for one to impose the usual boundary conditions. The other is the existence of interactions between the wave packet and obstacles in their way, where it becomes important to make the distinction if they are dielectric or conductors.

Considering all of that, an important phenomenon is the double-slit experiment, carried out by electrons moving across semiconductors. It was carried out for the first time using electrons in a vacuum in 1961 and has been repeated many times since. The other modality is that when the electrons move through a semiconductor which has further semiconductors inserted on it, that have a larger band gap. Thus, the energy of the moving electrons is not enough to move through an array of semiconductors, with a gap in between them.

In this kind of dispersion phenomena involving electrons, the material of the obstacles that are utilized to represent the slits matters. If it is dielectric, we can see an interaction between the electron charge and the electric dipoles that corresponds to the presence of walls interacting with moving charges. On the other hand, if the material is a conductor, one can see that the negative charges tend to move away from the electron cloud as it travels near them. In this case we see the rise of charge-charge interaction. The relevant aspect of this latter interaction is that it is five times more energetic than a dipole-dipole interaction. Also, the strength of the former has a longer range and loses intensity in the form, $\frac{1}{r^2}$ whereas the latter does so at $\frac{1}{r^6}$. In this last case, writing the Hamiltonian can be done without sacrificing considerable precision. However, when dealing with charge-charge interactions it is necessary to account for a term that includes an excess of positive charges in the conductor, that agglutinate near the slits. The situation becomes more complex when choosing the direction of an electron pulse because the positive charges of the conductive material get close to the slits and then return to reestablish electrostatic equilibrium.

The model being posed here has significance in the design of electronic devices at

the nanometric scale and the focus of the work on this thesis is the simplest form of the problem, which is with electrons moving through a vacuum. With this problem solved, it becomes feasible to tackle the complications mentioned previously, one by one. That is the purpose of Chapter 1.

The first chapter of this thesis is titled "Spatial and temporal description of electron diffraction through a double slit at the nanometer scale," [8] where the time dependent Schrödinger equation is used to solve the double-slit problem, that is represented as an electron pulse traveling towards a dielectric wall with two long, parallel slits.

The solution is obtained from an initial condition of a function $\psi(\vec{r}, t = 0)$, which is a gaussian probability amplitude.

The standard analytical framework [6] is not applicable in this case due to the following reasons:

- the slits are not infinitely thin. Their width plays a role in the phenomenon.
- the emission source is in such close proximity to the slits that it cannot be represented as a plane wave. Hence, what reaches the slits is a wavefront that still presents significant curvature and thus the hypothesis of the magnitude of the wave being the same in all points of the slit is unfulfilled.
- the detectors that make it possible to measure the diffracted pulse are so close to the slits that it is not possible to make the approximation of the wave length being too small compared to the distances involved between the slits and the detectors.

It is necessary to mention various aspects before explaining that we choose a specific physical system in the problem of electrons bound to a nanostructure because they are taken to be clusters of atoms that have been manufactured with different techniques. When nucleation takes place in gaseous phase, atoms aggregate as they move randomly throughout the gas. Under this circumstance it is possible that, before a cluster can be bound to an atom in direct manner, it is possible that it binds a single electron. Hence we are dealing with a kind of super atom where the electron follows the laws of quantum mechanics and has properties that can be studied. This thesis focuses on the case of a cluster with electric dipole moment in which one of its atoms has lost an electron. In this case, the work starts from a classical problem calculated by Sergio Gutiérrez López [22], who showed that one of these physical systems has an associated constant of motion, and, if an electric charge moves in its vicinity, then it can have stable orbits. Therefore, the quantum treatment of the problem is outlined as follows:

- What are the properties of a nanostructure after it became ionized and bound an electron to its periphery?
- The theoretical classical result opens the possibility that there exist quantum states of electrons bound to nanoparticles.
- If so, its energy spectra would give raise to electronic transitions with emission and absorption properties that can be observed so long as the half-lives of those states allow for it.

- In case of existing, the detection of an absorption-emission spectrum of light must depend on its intensity and, thus, on the quantity of ionized nanostructures, but this last aspect is left outside of the scope of this work.

The results are located in Chapter 2 of this thesis and correspond to the published paper titled "Bidimensional bound states for charged polar nanoparticles." [9] We also have obtained conclusive results for the tridimensional case.

The second objective consisted in generalizing the previous work to three dimensions. We obtained the classical form of a new constant of motion and found the quantum operator associated with it. We also solved the Schrödinger equation separating the angular part to demonstrate that the probability density slides towards the angle $\theta < \frac{\pi}{2}$. We studied the radial part and obtained the energies for the ground state and two excited states. We plotted the radial component of the wave function for a small electric dipole such as the cluster $(GaAs)_3$ and for very large electric dipoles such as fullerenes RbC_{60} and LiC_{60} .

The results were published in the academic paper titled "Behavior of an electron in the vicinity of a tridimensional charged polar nanoparticle through a classical and quantum constant of motion," [10] in the Journal of Nanoparticle Research.

SPATIAL AND TEMPORAL DESCRIPTION OF
ELECTRON DIFFRACTION THROUGH A
DOUBLE-SLIT AT THE NANOMETRE SCALE

1.1 Introduction

A numerical method is employed in order to study the time evolution of an electron wave packet that diffracts through a double slit at nanometric scale. The phenomenon of a wave packet in the vicinity of a double-slit is described. We explore the passing of the wave packet through the slits and how it diffracts. The dimensions of the setup are kept down to a hundred nanometers, meaning the common analytic approaches most used in the literature cannot be used.

The most common way of dealing with quantum diffraction is to use the Schrödinger equation, such that the Green function method is applied to obtain the Helmholtz-Kirchoff integral which is evaluated over a surface S_1 , though there is a different surface S_2 corresponding to the wave front of the packet. Many hypotheses must be introduced to calculate the Helmholtz-Kirchoff formula. These can be enumerated as follows: 1) if $|\vec{r}|$ is the distance from the point \vec{r} to S_2 , and λ is the wave length, it must be true that $|\vec{r}| \gg \lambda$. 2) The slit walls must be opaque and assumed to be infinitely thin, so as to avoid having to treat the apertures as channels where electrons traverse. 3) The integral is evaluated over S_1 which does not coincide with S_2 . 4) If \vec{r}_0 is any interior point to S_1 and $s = |\vec{r} - \vec{r}_0|$, it is postulated that $\{|\vec{r}, s|\} \gg \lambda$ to guarantee that $|ik| \gg \left\{ \frac{1}{s}, \frac{1}{|\vec{r}|} \right\}$.

Louis de Broglie presented the idea of the wave-like nature of corpuscles, he believed that the model of waves should be applied to both matter and radiation [17]. Operating in that context, he proposed the potential diffraction of electrons in crystals in order to test it. Davisson and Germer [16] measured experimentally, as documented by Gehrenbeck [20].

Quantum scattering has been studied with analytical and numerical approaches in the last decades [29, 32, 1, 43, 21, 33], but it could be helpful for undergraduate students to visualize its evolution in time by using images. In addition to that, particle diffraction experiments are available for electrons, neutrons, C_{60} fullerenes, and other systems, see for example [45, 4, 25]. It is clear from these developments that double slit phenomena are important not simply due to the conceptual aspects of quantum theory. Now it is known that it will be useful for new technologies, like the electron manipulation using laser beams in the vicinity of nanostructures, which could have interesting implications for fundamental technological research.

In this work, we solve the Schrödinger equation to study the temporal evolution of a gaussian wave packet that incides against a wall with two slits that are small compared to the dimensions of the region where the probability density of the outgoing packet is zero. The wall is represented with a potential $V(x, y)$ which is high enough to prevent tunneling effects. The numerical calculation relies on the method of finite differences in the time domain (FDTD) and is applied to a nondimensionalized form of the equation, in a rectangular grid. We obtain the time evolution of both the time amplitude and the probability density in the configuration space. Though in this chapter only four graphs are presented, it is possible to build an animation of the phenomenon that would have didactic utility. If the grid utilized in the numerical calculation consists of cells of 1 nm in length, the diffraction process takes place in 4.32×10^{-12} s. 26 cells of the computational space are chosen to serve as collectors, in an arrangement parallel to the double slit wall, where data is stored per every iteration of the algorithm. They are placed at a distance less than nine times the width of the slits to ensure a scheme that is not often considered in

conventional literature. When thinking of nanometric size devices, it is important to know the behavior of electrons in regions close to the walls.

These signals, collected at fixed regions, are time series whose Fourier transforms are calculated to plot the square of its absolute value. We take the wave function at fixed times and calculate the probability density in momentum space. We also modify the grid size to accommodate for micrometric scales, or greater. It is necessary to modify the length of time concerning the phenomenon under study.

1.2 Nondimensionalization, the FDTD method, and stability

We first used a process of nondimensionalization of the Schrödinger equation, in order to facilitate a finely tuned control of both the grid size and the algorithmic time steps. This allows us to shift calculations to a system of arbitrary units in space and time, that be easily manipulated to fit any scale in a straight forward manner simply by adjusting a set of constants.

1.2.1 Nondimensionalization and scale selection

Starting from the Schrödinger equation:

$$-\frac{\hbar^2}{2m_e}\nabla^2\psi(\vec{x},t) + V(\vec{x})\psi(\vec{x},t) = i\hbar\frac{\partial\psi(\vec{x},t)}{\partial t}, \quad (1.1)$$

where m_e is the electron mass, and $V(\vec{x})$ is the potential representing the double slit barrier

$$V(\vec{x}) = V_0 f(\vec{x}), \quad (1.2)$$

A change of scale is introduced:

$$\vec{x} = (x, y, z) = a\vec{\eta} = a(\eta_x, \eta_y, \eta_z), \quad (1.3)$$

where a is measured in meters, and $\vec{\eta}$ has no units. The Laplacian changes into: $\nabla^2 = \frac{1}{a^2}\nabla_{\vec{\eta}}^2$. Time also undergoes a change of scale as given by $t = \tau s$, which is measured in seconds, and where s also lacks units. By taking $\frac{2m_e a^2}{\hbar^2}V_0 = 3$ we obtain V_0 large enough to prevent tunneling effects through the potential walls. The following is also true: $a = \sqrt{\frac{3\hbar^2}{2m_e V_0}}$ and $\tau = \frac{2m_e a^2}{\hbar}$, in order to obtain an nondimensionalized form of the Schrödinger equation.

$$\nabla^2\psi(\vec{\eta},s) - f(\vec{\eta})\psi(\vec{\eta},s) = -i\frac{\partial\psi(\vec{\eta},s)}{\partial s}, \quad (1.4)$$

The stability condition is

$$\Delta s \leq r_a(\Delta\eta_x)^2, \quad (1.5)$$

In this chapter $f(\vec{x})$ is given by:

$$f(\vec{x}) = \begin{cases} 3, & 1 \leq x \leq x_1, \quad x_2 \leq x \leq x_3, \quad x_2 \leq 1 \leq x \leq L_1; \\ & y_1 \leq y \leq y_2; \\ 0, & \text{otherwise,} \end{cases}$$

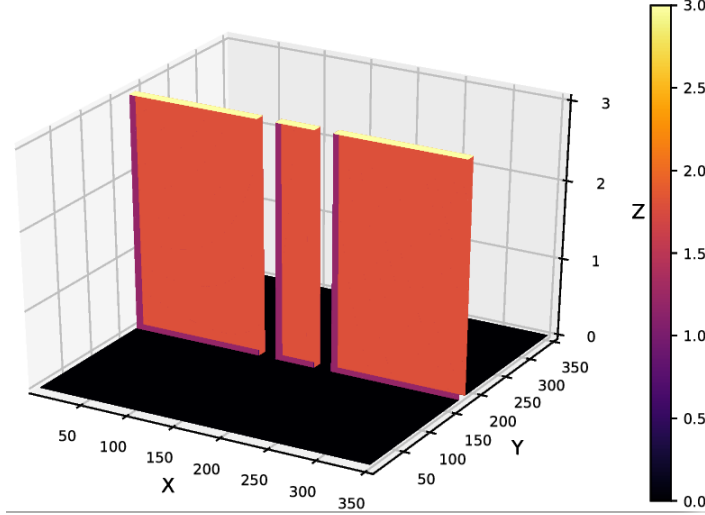


Figure 1.1: Spatial representation of the potential barrier, $f(\vec{x})$.

where $x_1 = 136$, $x_2 = 156$, $x_3 = 196$; $y_1 = 171$, $y_2 = 181$. The dimensions of the box are $L_1 = L_2 = 351$. $V_0 = 0.1143$ eV. This function is represented by the Figure 1.1.

This scale shift makes it easier to work in the nanoscale by taking $a = 1 \times 10^{-9}$ m. In this case $\tau = 1.7276 \times 10^{-14}$ s and $V_0 = 0.1143$ eV, so that $\Delta t = \tau \Delta s = 2.1595 \times 10^{-15}$ s. The solution is expressed in algorithmic time. In order to relate it with real time, it is enough to multiply it by the constant $t = 2.1595$ fs.

It is possible to produce the diffraction of particle beams using neutrons, atoms, molecules, C_{60} fullerenes, etc[47][7][3][31].

For the potential barrier shown in Figure 1.1 in this work, it is possible to run a simulation completely at the nanoscale range. We set the scale by evaluating $a = 1$ nm. From there we can set the mass m of the diffracted particle of our choosing. For this chapter, we are working with the electron mass. We set the de Broglie wavelength λ . The initial wave packet is determined in this way. The value of τ is straightforward too.

1.2.2 The FDTD method

The finite difference in the time domain method was introduced by Kane Yee in 1966[46] in order to solve Maxwell's equations but it can also be used to solve the Schrödinger equation[30][44][35][36][37][38], which is what we do in this work. For the one dimensional case

$$i\hbar \frac{\partial \psi(x, t)}{\partial t} = -\frac{\hbar^2}{2m} \frac{\partial^2 \psi(x, t)}{\partial x^2} + V(x)\psi(x, t), \quad (1.6)$$

where we propose a solution of the form:

$$\psi(x, t) = \psi_1(x, t) + i\psi_2(x, t). \quad (1.7)$$

By direct calculation, one obtains the following equations:

$$\hbar \frac{\partial \psi_1(x, t)}{\partial t} = -\frac{\hbar^2}{2m} \frac{\partial^2 \psi_2(x, t)}{\partial x^2} + V(x)\psi_2(x, t), \quad (1.8)$$

$$-\hbar \frac{\partial \psi_2(x, t)}{\partial t} = -\frac{\hbar^2}{2m} \frac{\partial^2 \psi_1(x, t)}{\partial x^2} + V(x)\psi_1(x, t), \quad (1.9)$$

Where the solution will be located in the interval: $0 \leq x \leq L$, as well as a partition

$$\Delta x = \frac{L}{N}, \quad (1.10)$$

where N is a natural number.

In order to discretize time for (1.8), we use the following partition:

$$\{0, \Delta t, 2\Delta t, \dots, n\Delta t\}$$

Equation (1.9) is discretized using the next partitioning scheme:

$$\left\{ \frac{1}{2}\Delta t, \frac{3}{2}\Delta t, \dots, \left(n + \frac{1}{2}\right)\Delta t, \dots \right\}$$

The potential $V(x)$ is evaluated at each point and denoted as $V_j = V(j\Delta x)$.

Discretizing the derivatives in space and time:

$$\frac{\partial^2 \psi(x, t)}{\partial x^2} \simeq 8 \frac{1}{\Delta t} [\psi(x + \Delta x, t) - 2\psi(x, t) + \psi(x - \Delta x, t)], \quad (1.11)$$

$$\frac{\partial \psi(x, t)}{\partial t} \simeq \frac{1}{2\Delta t} [\psi(x, t + \Delta t) - \psi(x, t - \Delta t)] \quad (1.12)$$

For ease of notation and calculations we use

$$\psi(j\Delta x, n\Delta t) = \psi_j^n. \quad (1.13)$$

Once discretized, the equations for (1.8) and (1.9) take the form

$$(\psi_1)_j^{n+1} \simeq (\psi_1)_j^n - \frac{\hbar \Delta t}{2m(\Delta x)^2} [(\psi_2)_{j+1}^{n+\frac{1}{2}} - 2(\psi_2)_j^{n+\frac{1}{2}} + (\psi_2)_{j-1}^{n+\frac{1}{2}}] + \frac{\Delta t}{\hbar} V_j (\psi_2)_{j-1}^{n+\frac{1}{2}}, \quad (1.14)$$

$$(\psi_2)_j^{n+\frac{1}{2}} \simeq (\psi_2)_j^{n-\frac{1}{2}} + \frac{\hbar \Delta t}{2m(\Delta x)^2} [(\psi_1)_{j+1}^n - 2(\psi_1)_j^n + (\psi_1)_{j-1}^n] + \frac{\Delta t}{\hbar} V_j (\psi_2)_j^n. \quad (1.15)$$

The purpose of this formulation is to calculate the values of ψ_1 from initial values of ψ_2 , and to use the latter to recalculate ψ_1 and repeat the succession over algorithmic time until a run is finished, as shown in Figure 1.2.

The equation in two dimensions is solved in a similar manner. The algorithmic time was chosen to end at a specific point when the wave front has not reached the walls yet; also, a sufficiently large L was chosen in order to minimize their effect. That is how we avoided the inclusion of absorbing boundary conditions whose calculation complicates the algorithm needlessly.

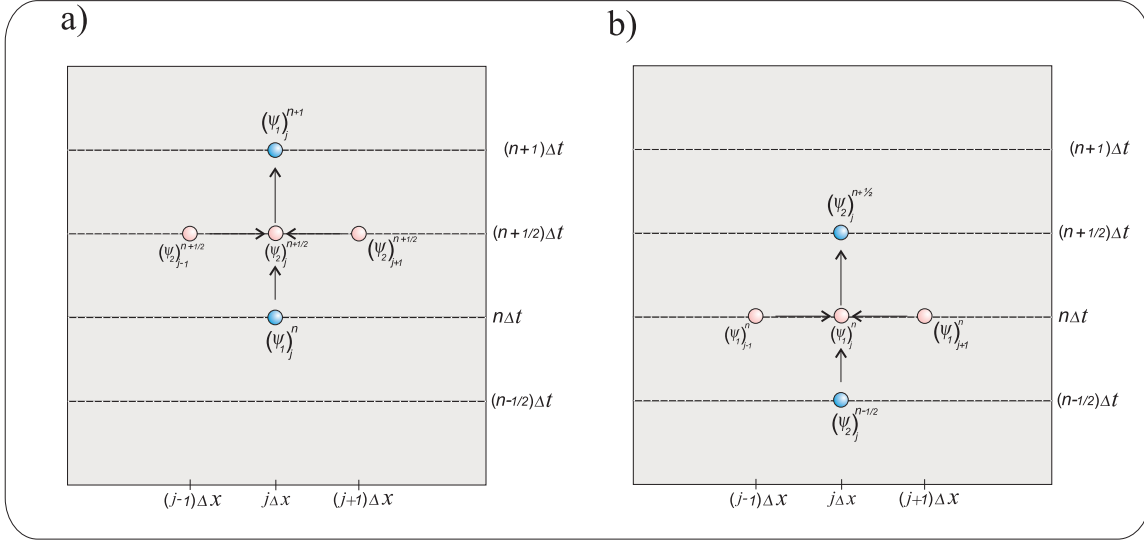


Figure 1.2: Visualization of the temporal discretization scheme. The real and imaginary components are shifted in time by $\frac{1}{2}\Delta t$. The updating of ψ_1 depends on ψ_2 and viceversa. a) Update diagram of ψ_1 using (1.14), b) Update diagram of ψ_2 using (1.15).

1.2.3 Stability conditions

One can say that, in finite difference approximations, the algorithm is stable so long as truncation errors, round-off, etc. decay from one time step to the next. This can be explained in one dimension, in a grid with time steps $n\Delta t$ in the vertical axis and the spacial steps Δx in the horizontal axis. The propagation of the solution must be such that the wave front reaches each horizontal line of the grid before the vertical ones. In an algebraic way, it means that $v_g\Delta t < \Delta x$. Therefore, a relation between the spatial and temporal discretizations is necessary in order to keep the numerical error under control. This is done by Soriano et al.[34] by separating the Schrödinger equation in two eigenvalue problems, spatial and temporal:

$$i\hbar\frac{\partial\psi}{\partial t} = \lambda\psi, \quad \hat{H}\psi = \lambda\psi.$$

The points of the grid can be defined as: $(n\Delta t, j\Delta x, r\Delta y, s\Delta z)$ with n, j, r, s , being four non negative integers. The function $\psi(n\Delta t, j\Delta x, r\Delta y, s\Delta z)$ is denoted as $\psi^n(j, r, s)$. The temporal derivative is discretized to find

$$\frac{i\hbar}{\Delta t} \left[\psi^{n+\frac{1}{2}}(j, r, s) - \psi^{n-\frac{1}{2}}(j, r, s) \right] = \lambda\psi^n(j, r, s)$$

A growing factor is defined as $q = \frac{\psi^{n+\frac{1}{2}}(j, r, s)}{\psi^n(j, r, s)}$, and the last discretization is written as a second degree equation

$$q^2 + i\frac{\Delta t\lambda}{\hbar}q - 1 = 0$$

It must be noted that λ is real because $i\hbar\frac{\partial}{\partial t}$ and \hat{H} are hermitian operators. So, the solution can produce $q = \frac{\psi^{n+\frac{1}{2}}(j, r, s)}{\psi^n(j, r, s)} < 1$ if $\frac{\lambda\Delta t}{2\hbar} < 1$. A wave packet can be expressed as a linear combination of plane waves so that $\psi^n(j, r, s)$ can be written as follows:

$$\psi^n(j, r, s) = Ae^{i(jk_x\Delta x + rk_y\Delta y + sk_z\Delta z - n\omega\Delta t)}.$$

The discretization of the second derivative is of the form

$$\frac{[\psi^n(j, r, s)]''}{\psi^n(j, r, s)} \simeq \frac{\sin^2(\frac{k_x \Delta x}{2})}{(\Delta x)^2},$$

where $[\psi^n(j, r, s)]''$ is the second spatial derivative. The eigen-value problem produces the relation:

$$\lambda \simeq -\frac{[\psi^n(j, r, s)]''}{\psi^n(j, r, s)} + V \simeq \frac{2\hbar^2 \sin^2(\frac{k_x \Delta x}{2})}{m (\Delta x)^2} + V.$$

Its generalization to three dimensions produces

$$\frac{2\hbar}{\Delta t} > \frac{2\hbar^2}{m} \left[\frac{\sin(\frac{k_x \Delta x}{2})}{(\Delta x)^2} + \frac{\sin(\frac{k_y \Delta y}{2})}{(\Delta y)^2} + \frac{\sin(\frac{k_z \Delta z}{2})}{(\Delta z)^2} \right] + V.$$

Taking the maximum absolute value of the potential V_{max} , and considering that $\sin(\alpha)^2 < 1$, a simple inequality is proposed:

$$\frac{2\hbar}{\Delta t} > \frac{2\hbar^2}{m} \left[\frac{1}{(\Delta x)^2} + \frac{1}{(\Delta y)^2} + \frac{1}{(\Delta z)^2} \right] + V_{max}.$$

1.3 Physical System

We solved the Schrödinger equation numerically. The values of the parameters were chosen to work at the nanoscale. The system consists of a wall with a double-slit.

The incident electron wave packet is specified as

$$\psi(x, y, t = 0) = N e^{-\frac{1}{2}(\frac{x-x_0}{\sigma_x})^2 - \frac{1}{2}(\frac{y-y_0}{\sigma_y})^2} e^{i[\frac{2\pi}{\lambda} \vec{k} \cdot (\vec{x} - \vec{x}_0)]}, \quad (1.16)$$

where x_0 and y_0 are the starting location of the center of the wave packet at time $t = 0$, which will be sent from the middle of the grid in the direction $\vec{k} = k\hat{n} = \frac{2\pi}{\lambda}(0, 1)$. A one-dimensional version of this wave packet is analyzed by Cohen-Tannoudji, et., al.[11] They consider the superposition of plane waves in configuration space:

$$\psi(x, t) = \frac{\sqrt{a}}{(2\pi)^{\frac{3}{4}}} \int_{-\infty}^{\infty} e^{-\frac{\alpha^2}{4}(k-k_0)^2} e^{i[kx - \omega(k)t]} dt$$

with $\omega(k) = \frac{\hbar k^2}{2m}$. Evaluating the integral defines the wave packet as

$$\psi(x, t) = \left(\frac{2a^2}{\pi}\right)^{\frac{1}{4}} \frac{e^{i\phi}}{[a^4 + \frac{4\hbar^2 t^2}{m^2}]^{\frac{1}{4}}} e^{ik_0 x} e^{-\frac{(x - \frac{\hbar k_0 t}{m})}{(a^2 + 2i\frac{\hbar t}{m})}},$$

so that when comparing the well known normal distribution function with the probability density $\rho(x, t) = |\psi(x, t)|^2$, one finds that the wave packet moves with the speed $\frac{\hbar k_0}{m}$ and its standard deviation grows as follows

$$\sigma(t) = \sigma_0 \left[1 + \frac{\hbar^2 t^2}{4\sigma_0^2 m^2} \right]^{\frac{1}{2}},$$

where σ_0 is the standard deviation at time $t = 0$. Since the coefficient of t is very large, the numerical simulation must exhibit spreading even for short times.

Since the wave function must remain normalized at all times, it served an important purpose in this work. We calculated the normalization constant N in order to carry out a normalization check of the wave function, before applying the FDTD method. The procedure was repeated after the last iteration concluded, in order to verify that the algorithm remained stable throughout the whole run.

The parameters utilized were the following: $\lambda = 12, 16$, $\Delta\sigma_x = \sigma\eta_y = 1$, $r_a = 1.8$ (stability parameter), and $\Delta s = r_a(\Delta_x)^2$ which is the time between iterations of the algorithm.

The flux velocity of the wave packet is

$$\vec{v} = \frac{i\hbar}{2m_e} \left(\frac{\nabla\psi^*}{\psi^*} - \frac{\nabla\psi}{\psi} \right) = \frac{i\hbar}{2m_e} (0, -2ik). \quad (1.17)$$

Evaluated with $\lambda = 12$ nm produces

$$\vec{v} = \hat{y} \frac{\hbar}{m_e} \frac{2\pi}{\lambda} = 6.0616 \times 10^4 \frac{m}{s} \hat{y}, \quad (1.18)$$

and the energy is

$$\epsilon = \frac{1}{2} m_e v^2 = 1.0445 \times 10^{-2} \text{ eV}. \quad (1.19)$$

This is a magnitude 9 times the potential V_0 , as mentioned in the nondimensionalization section. To the knowledge of the authors, electron beams can be produced with an intensity of 1eV [28]. If the time unit is Δt , every increment in frequency will be $\Delta\nu = \frac{1}{\Delta t} = 7.0659 \times 10^{9\frac{1}{s}}$. That way, the energy counts are multiples of the magnitude $\Delta\epsilon = h\Delta\nu = 2.92 \times 10^{-5}$ eV.

The numerical solution seeks to model a physical system in which an electron wave packet is sent in the vertical direction from the position $\vec{x} = (x_0, y_0)$. The walls that the wave packet will interact with are represented as a potential in the Schrödinger equation. It has two slits in the \hat{z} direction. In this way, the problem will be studied in a bidimensional box where x is the horizontal axis and y is the vertical axis. We choose twenty six cells where changes we will store the values of the wave function over time, where the data will be stored in separate files.

Going forward, we will refer to these cells as collectors. These will be used to store the probability density data and its behavior as it moves through the system, as it passes through the locations corresponding to the cells. As shown in the figure, twenty six collectors are placed on the opposite side of the two slits, at $y = 380$ nm, covering the cells marked by \vec{x}_j , with $j = 1, \dots, 26$, separated a distance $\delta\eta = 6$ nm. The presence of the wave packet will be registered in each of them. There, $\psi(\vec{x}_j, t) = \psi_r(\vec{x}_j, t) + i\psi_{im}(\vec{x}_j, t)$ will be recorded as it makes its way through, increasing in intensity over time. The wave function $\psi(\vec{x}_j, t) = \psi_r(\vec{x}_j, t) + i\psi_{im}(\vec{x}_j, t)$ will be recorded as it makes its way through the collectors, where they will record the values that it takes over time will be recorded and stored until the wave packet has left completely.

The dimensions of the barrier are: width $h = 10$ nm, the slits are 20 nm long, and their separation is 120 nm. The experimental arrangement of the physical system is set up as shown in Figure 1.3.

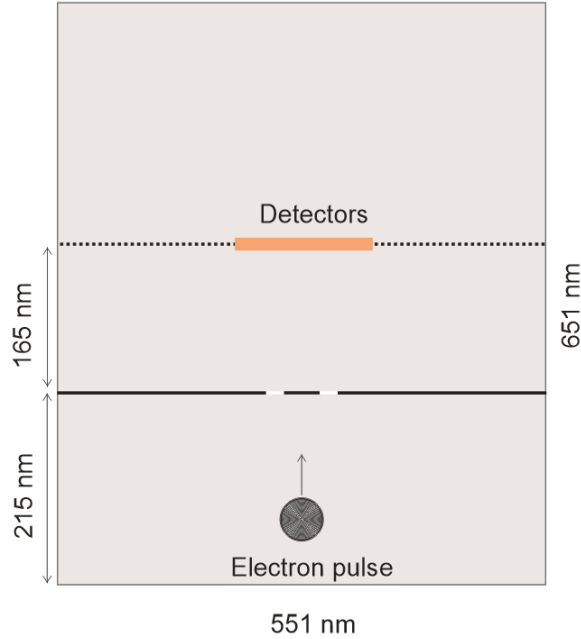


Figure 1.3: Spatial arrangement of the numerical space. The width of the box is 551 nm and its height 654 nm. Using $\tau = 1.7276 \times 10^{-14}$ s. The double-slit wall is located 215 nm from the origin, and the collector line is placed 165 nm from the wall. The wave packet travels from the lower part in the vertical direction. The vertical width of the wall is $h = 10$ nm. The width of each slit is 20 nm.

1.4 Numerical Results

The results presented in this section are organized as follows: ψ and ρ are plotted in the configuration space at different times, more specifically in subsection 1.4.1. The time evolution of the wave packet is recorded for said times at several fixed regions (specific cells of the grid), and their Fourier transforms are presented in subsection 1.4.2. Representation in momentum space is shown in subsection 1.4.3.

1.4.1 Configuration Space

A solution of the Schrödinger equation in the numerical space is found for every iteration of the FDTD algorithm. We obtain the values for the wave function $\psi(x, y, t)$ and for the probability density $\rho(x, y, t) = |\psi(x, y, t)|^2$. The algorithmic time will be denoted as T from now on.

It is possible to observe the dispersive behavior of the probability density as it moves forward and approaches the vicinity of the walls. This is shown in Figure 1.4 on the left, at $T = 165$ which corresponds to $t = 0.356$ ps; and on the right, at $T = 700$, which corresponds to $t = 1.512$ ps.

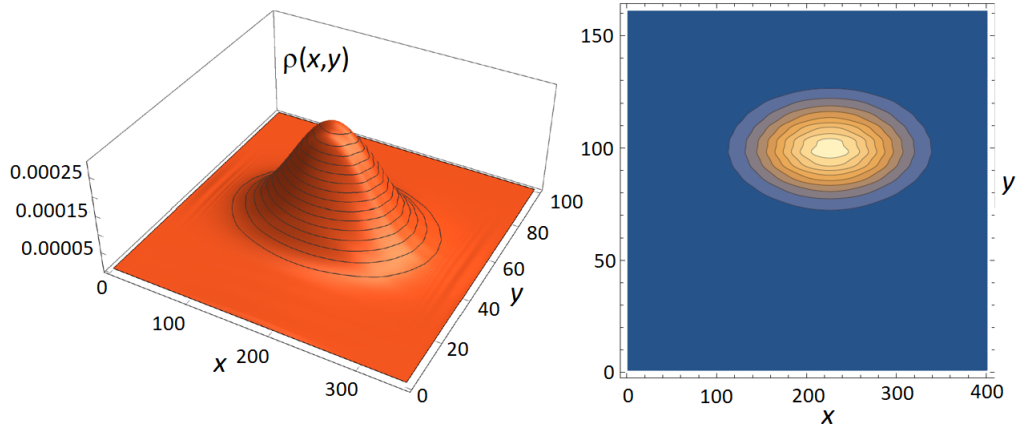


Figure 1.4: Shape of the wave packet before diffraction. Left: $|\psi(\vec{x}, T = 165)|^2$, $T = 165$, which is equivalent to $t = 0.356$ ps. Right: wave packet at $T = 700$, which is equivalent to $t = 1.51$ ps. The wave packet undergoes gradual dispersion over time.

The wave packet crossing the double-slit can be appreciated in Figure 1.5 on the left, at $T = 1020$, which corresponds to $t = 2.203$ ps. The wave-like nature of the phenomenon presents itself almost immediately at $T = 1225$, which corresponds to $t = 2.710$ ps. This is when the interference pattern starts to appear.

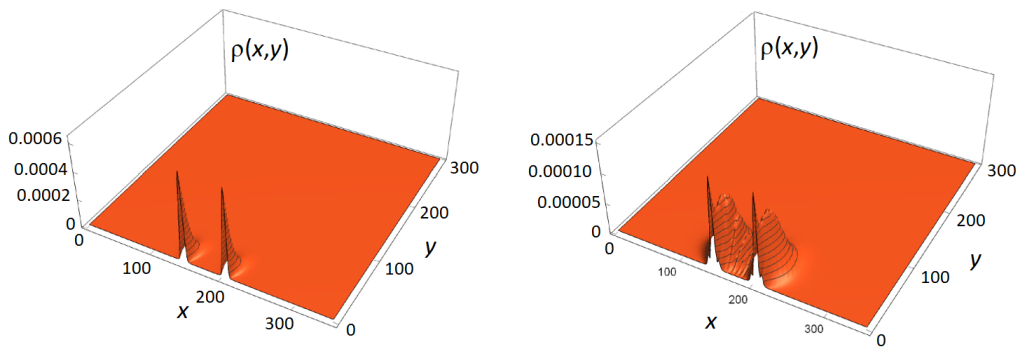


Figure 1.5: Appearance of interference pattern in the probability density, the potential is situated at $y = 0$. Left: at $T = 1020$, which corresponds to $t = 2.203$ ps. It forms two peaks as it passes through the double slit. Right: at $T = 1255$, which corresponds to $t = 2.710$ ps, where the beginning stages of the interference pattern appear.

The shape of the interference pattern appears very early on, as shown in Figure 1.6. The times are $T = 1495 = 3.228$ ps, and $T = 1605 = 3.466$ ps.

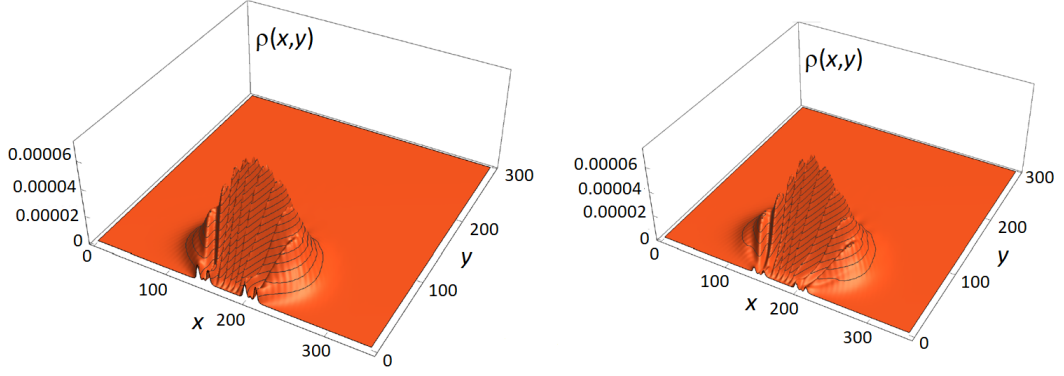


Figure 1.6: Formation of the interference pattern in $|\psi(\vec{x}, T)|^2$, the potential is situated at $y = 0$. Left: pattern at $T = 1495$, which correspond to $t = 3.228$ ps. Right: pattern at $T = 1605$, which correspond to $t = 3.466$ ps.

Focusing on the line $y = 0$, we can visualize a closer relationship between the numerical results and the figures most commonly found in the literature as shown in Figure 1.7. The difference in our work is that the initial wave packet is not an incident plane wave nor is the magnitude of the distance of the observation screens necessarily too far away, compared to the dimensions of the slits. The behavior can be mapped at any region and at any time of our choosing.

Each one of the collectors corresponds to an incident signal over a square surface whose edge length is 1 nm and are placed along the $y = 380$ nm line, where they will record the values of the probability density in place. They are twenty six in total and are placed 6 nm apart, their positions are denoted as \vec{x}_k , with $j = 1, 2, \dots, 26$. The line is located 165 nm away from the double slit wall, as seen in Figure 1.8. Four algorithmic times were chosen in order to compare the behavior of the probability density: $T_1 = 1255 = 2.71$ ps, $T_2 = 1459 = 3.15$ ps, $T_3 = 1900 = 4.10$ ps, and $T_4 = 2000 = 4.32$ ps. Taking these times into account, we find that the displacement of the probability density in the direction parallel to the wall is extremely fast.

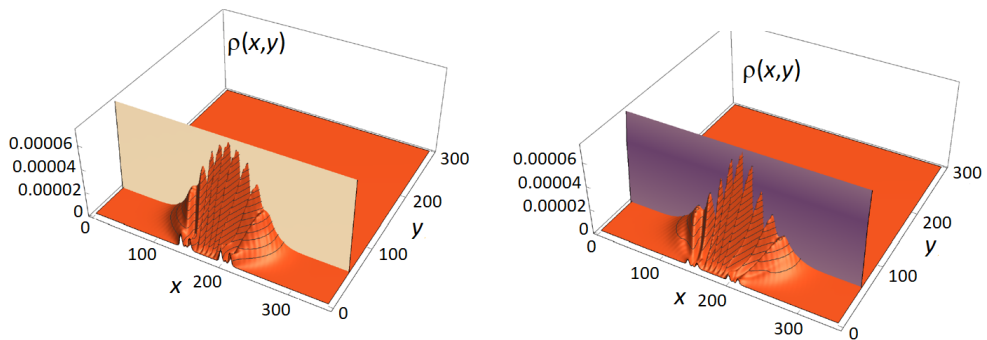


Figure 1.7: Intersection of $|\psi(\vec{x}, T)|^2$ with a plane parallel to the double slit, where the position of the potential wall is at $y = 0$. This depiction is analogous to electron intensities hitting a screen.

The displacement of probability density in the direction parallel to the wall is extremely fast.

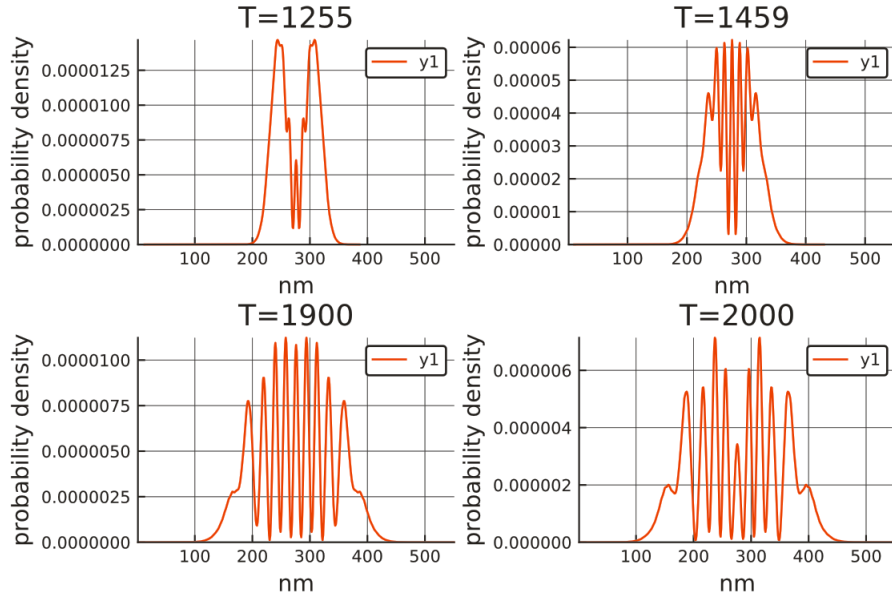


Figure 1.8: Intersection curves of $|\psi(\vec{x}, T)|^2$ with a plane parallel to the wall, placed at $y = 380 \text{ nm}$. The times are: $T = \{1255, 1459, 1900, 2000\}$, which in real time correspond to $t = \{2.71, 3.15, 4.10, 4.32\}$ ps. Probability currents are discernible in the in the horizontal axis.

1.4.2 Collection at fixed points through time and comparison of local information

The study at fixed points is developed working with the same collectors. They are used to study the probability density as it passes through them. The value of the wave function $\psi(\vec{x}_j, t)$ is stored in each \vec{x}_j at every iteration of the algorithm. This is how the probability density, $\rho(\vec{x}_j, t) = |\psi(\vec{x}_j, t)|^2$, is stored over time. It is analogous to an audience at a theater listening to music at different \vec{x}_k locations, where sound waves will reach them where they sit for the duration of the melody. Figure 1.9 shows the results for three signals. They correspond to the collectors placed at $k = 0, 5, 11$. It can be inferred from the plot that, for each collector, the wave packet will take at least $T = 1500 = 3.24$ ps.

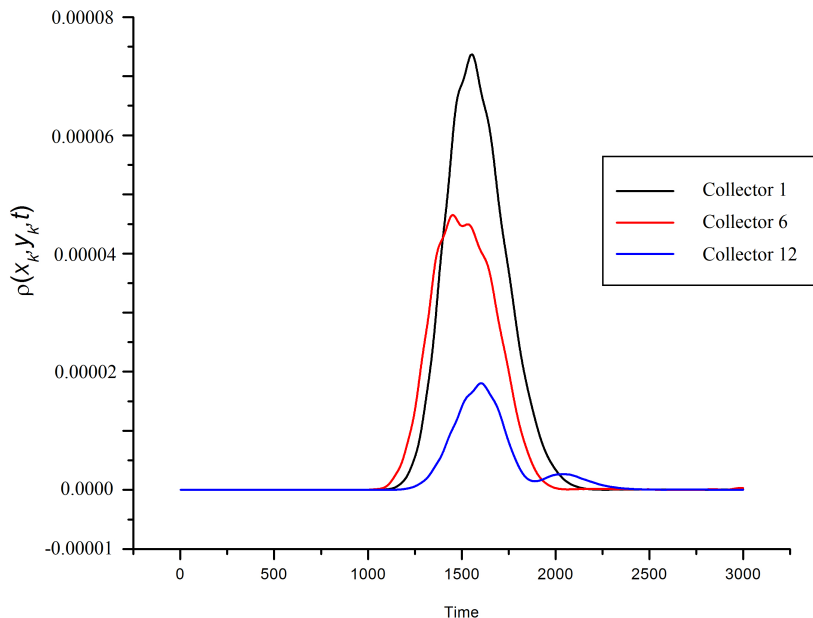


Figure 1.9: Data as recorded by the collectors. It shows how the probability density increases and then diminishes over time, as the wave packet passes through them. The collectors are placed at $x = 276$ nm, $k = 0, 1, \dots, 13$; located over a line placed 65 nm ahead of the wall.

As expected, the maximum signal values from the twenty six collectors also follow a diffraction pattern, as shown in Figure 1.10:

The absolute value of the square of the Fourier transform $|\phi(\vec{x}_j, \omega)|^2$ for every collector can be calculated from $\psi(\vec{x}_j, t)$, by using the numerical version of the expression $\phi(\vec{x}_j, \omega) = \frac{1}{2\pi} \int_{-\infty}^{\infty} \psi(\vec{x}_j, t) e^{-i\omega t} dt$. Maxima were calculated for each collector and they, again, show a diffraction pattern similar to the one corresponding to the probability densities $\rho(\vec{x}_j, t)$. The results are shown in Figure 1.11.

The structure of $|\phi(\vec{x}_j, \omega)|^2$ shows that the lowest frequencies are the most dominant. The cases chosen were for $j = 0, 5, 11$ which appear in Figure 1.12 (left). This suggests that for $\lambda = 12$ nm, the energy of the wave packet (1.0445×10^{-2} eV) disperses in space while diffraction takes place. This means that the energy in each collector is $\epsilon_1 = 2.92 \times 10^{-5}$ eV. The relative importance of the higher energies

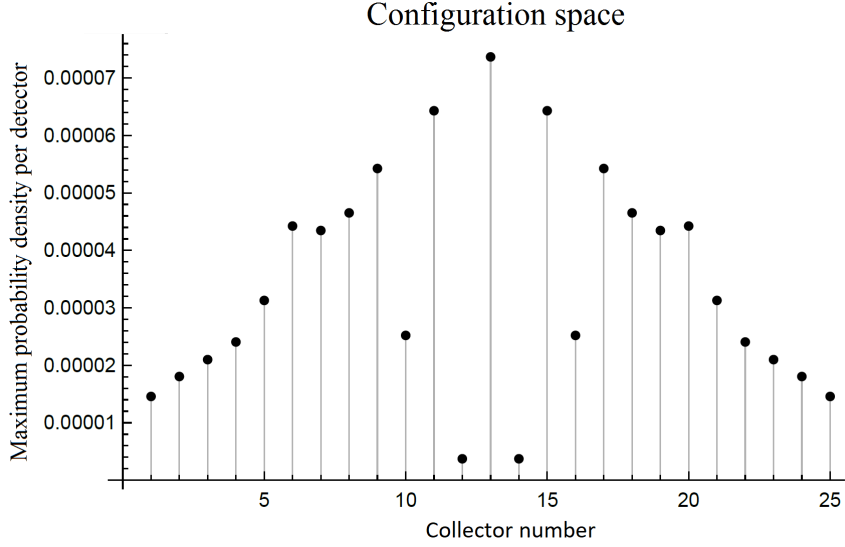


Figure 1.10: Depiction of the maxima $|\psi(\vec{x}_k, T)|_{max}^2$, as recorded by the collectors in configuration space. It follows an interference pattern.

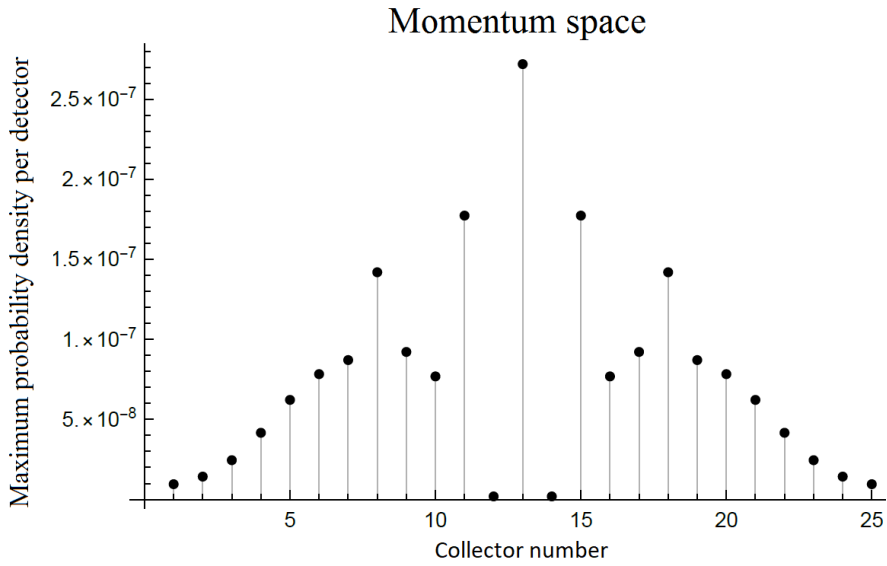


Figure 1.11: Maxima of the at fixed points in momentum space of the probability density $|\phi(\vec{x}_j, \omega)|_{max}^2$. It also follows an interference pattern.

$(\epsilon_n = n\epsilon_1)$ decreases in a way that the relative weight for $\epsilon_9 = 9\epsilon_1$ is 2.47496×10^{-3} with respect to ϵ_1 . Also, the right tail of the right hand side of the frequencies plot represents magnitudes of $|\phi(\vec{x}_j, \omega)|^2$, whose relative importance is of the order of 1×10^{-11} with respect to ϵ_1 . These peaks are located in frequencies that correspond to the energies between 4.6 meV and 6.57 meV, as shown in Figure 1.12.

The phenomenon of diffraction through the double-slit is such that the frequency spectrum of the wave packet is distributed through space. This means that all collectors receive different signals.

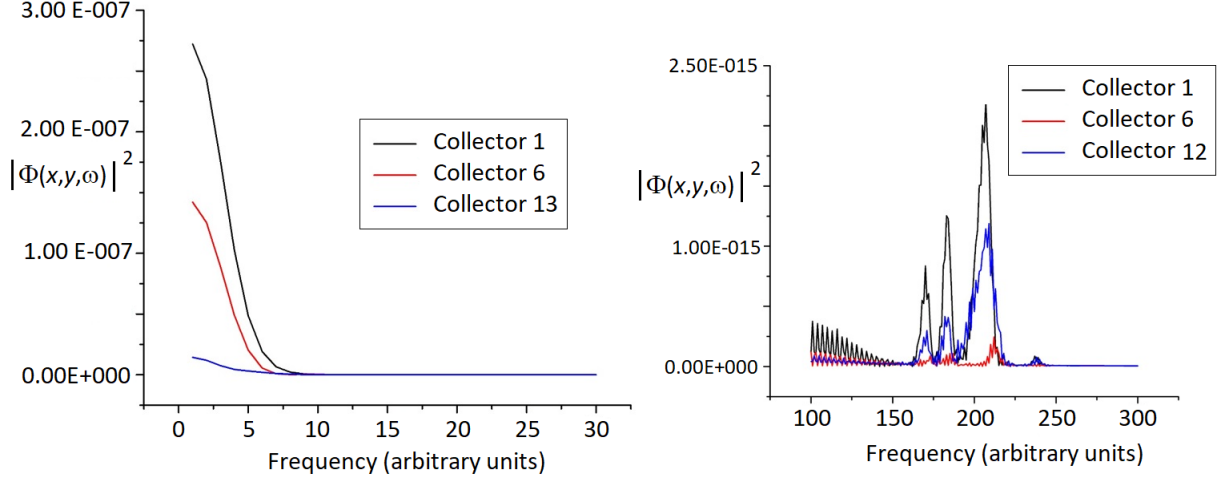


Figure 1.12: Left: depiction of the magnitude of the square of the absolute value of the Fourier transform $|\phi(\vec{x}_j, \omega)|^2$ with respect to ω . It takes its more significant values at lower frequencies. Right: local peaks appear for higher energies but they are practically irrelevant.

1.4.3 Momentum space

The probability density in momentum space $|\phi(k_x, k_y, t_k)|^2$ for fixed times t_k is evaluated using the expression $\phi(\vec{k}, t_j) = \frac{1}{\sqrt{(2\pi)^2}} \int_{-\infty}^{\infty} \int_{-\infty}^{\infty} \psi(\vec{x}, t) e^{-\vec{k} \cdot \vec{x}} dx dy$. The wave numbers k_x and k_y are expressed in arbitrary units and we pay particular attention only to the activity taking place in a line parallel to the wall with the double-slits. At first glance, the study is complicated due to the apparent absence of quantitative differences, as can be appreciated in Figure 1.13 recorded at $T_1 = 1255 = 2.71$ ps and $T_2 = 1605 = 3.47$ ps.

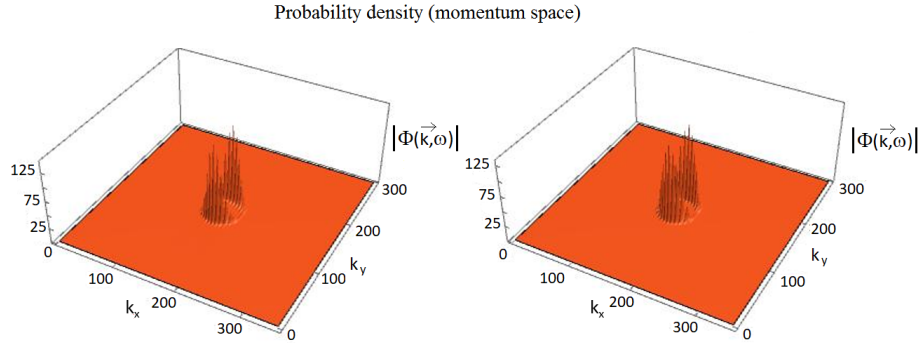


Figure 1.13: Depiction of the probability density $|\phi(\vec{k}, \omega)|^2$ in momentum space. Left: for $T = 1255$, which corresponds to $t = 7.71$ ps. Right: for $T = 1605$, which corresponds to $t = 3.47$ ps. There is no apparent change from one time to the next.

To find the differences, we analyzed specific values k_y of the function ϕ with k_x as the single variable, and observed an interesting underlying dynamic of the probability distribution.

The behavior of the probability density in momentum space is revealed using time analysis of the evolution of $|\phi(k_x, k_y, t_j)|^2$ and comparing at different times t_j . It is compared at times $T_j = 165 = 0.36$ ps and $T_j = 915 = 1.98$ ps. In both cases the wave packet does not reach the wall with the double-slits, thus diffraction has not begun yet. A comparison is made for $k_y = 130, 140, 160$. In the three cases in Figure 1.14, where the corresponding curves are superimposed, we found that no changes are appreciable within the precision allowed by the numerical method.

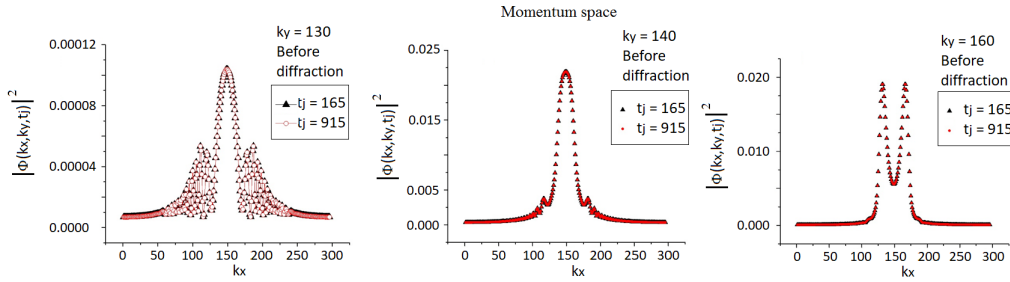


Figure 1.14: Depiction of the probability density $|\phi(k_x, k_y, t_j)|^2$ in momentum space as would be seen on perpendicular planes intersecting at $k_y = 130, 140, 160$. The curves are plotted against two distinct times t_j . As far as the precision of the numerical method allows, no changes occurred.

It is a different situation when the wave packet is in the process of crossing through the double slit, recorded at $T_j = 915$, and $T_j = 1020 = 2.2$ ps. A series of notable changes can be seen during this time interval, as shown in Figure 1.15.

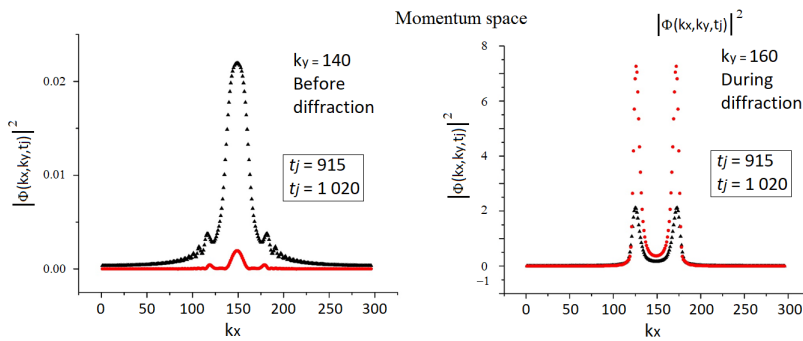


Figure 1.15: Depiction of the probability density $|\phi(k_x, k_y, t_j)|^2$ in momentum space on perpendicular planes intersecting at $k_y = 140, 160$ at two distinct times t_j . Now changes are easily discernible, with the momenta changing drastically from one time to the next.

Paying attention on the line $k_y = 140$, we see that the probability density in momentum space has a high value at time $T_j = 915$, and reduces significantly at $T_j = 1020$. On the other hand, in line $k_y = 160$, the opposite is true: the probability density is small in $T_j = 915$, and considerably increases at $T_j = 1020$. Therefore, as diffraction evolves, we see that there is a probability shift in the region over the line $k_y = 140$ to the line $k_y = 160$. This is a generalized phenomenon showing that the values of the probability density are appreciably distinct from zero, meaning there is a considerable shift in the values of the momenta.

1.5 Conclusions

This chapter studies the time evolution of an electron wave packet of initial Gaussian probability distribution with a plane wave factor.

The incident wave packet interacts against a wall with two slits that are very large compared with the dimensions of the region where it scatters. The approach used in this work provides new insights in diffraction of electrons through a double slit. We nondimensionalized the Schrödinger equation so we could work with different scales in a more straightforward manner. Our interest lies in studying the region close to where the diffraction phenomenon takes place. For that purpose, data is recorded for fixed instants, at times when the diffracted wave packet has not traveled too far compared to the size of the slits, meaning that the probability density $\rho(\vec{x}, t)$ is different from zero at points not farther than ten times the value of the width of the slits. We solved the Schrödinger equation using the FDTD method, and recorded the solution in different ways: 1) at fixed times t_k , in order to obtain the spatial distribution $\rho(\vec{x}, t) = |\psi(\vec{x}, t_j)|^2$, and 2) at fixed \vec{x}_k points, so as to record the evolution of the wave packet by the collectors in the different regions that they occupy, recording $\rho(\vec{x}_k, t)$. Fourier transforms were calculated for both cases and its results analyzed. By taking the size of a square cell to be that of 1 nm per side, it turns out that the phenomenon as a whole occurs in less than 4.32 ps, and the interference pattern appears only 0.5 ps after the wave packet crosses the double slit. Horizontal parallel lines to the wall were traced in order to reveal the existence of oscillatory behavior in that direction, modifying the probability density alongside it quickly and showing that we are not dealing with a stable pattern of interference, which is the case of observations concerning far fields. The collected signal at the collectors shows that the entirety of the wave packet passes through them in less than 3.24 ps. As expected, when comparing the maxima achieved by the probability density. The collection of peaks are similar to the interference pattern, and the same holds for the Fourier transforms ($|\phi(\vec{x}_k, t)|^2$). From these results, it is clear that the probability density $|\rho(E)|$ decreases as the energy increases. We obtained the momentum space representation via the Fourier transform of the wave function $\psi(\vec{x}, t_j)$, and is denoted as $\phi(\vec{x}, t_j)$, and it is such that the square of its absolute value also reveals vigorous dynamics so that in the regions near where the diffraction phenomenon is taking place, the probabilities undergo a spatial redistribution that has a corresponding equivalent in the momentum space.

This treatment can be extended to the study of the behavior of a wave packet of electrons inside semiconductors by using the concept of effective mass.

1.5.1 Conceptual exercise

The interested reader can study diffraction of a wave packet that can correspond to different particles that move in space at either nanometric or micrometric scales. The mass M is set, fixing the type of particle. By setting the value of a is how dimensions are set. The value of V_0 is necessary to avoid tunneling through the potential, which is obtained using the expression presented at the end of the section 1.2.1. The value of the parameter τ relates to the algorithmic time with real time, and is determined automatically after setting M and a .

Several projects can be developed by students at the undergraduate level. We

suggest working with a potential given by the expression:

$$V(x, y) = V_0 e^{-\frac{(x-x_0)^2}{2\sigma_x^2} - \frac{(y-y_0)^2}{2\sigma_y^2}} \quad (1.20)$$

Using values where $V_0 > 0$ one can plot images in which diffraction becomes evident as the wave packet splits upon reaching the potential, and this can be discussed in class. For $V_0 < 0$, the effect differs, and the packet sinks inside of the potential and is then shot forward in a concentrated form.

1.5.2 About the computer program

For this paper, the Schrödinger equation was solved via the FDTD method using a program written in the Julia programming language[5]. Time was discretized in M time steps with a separation of Δt between each. The solution consists of a set of files saved each iteration t_k , where $k = 1, 2, \dots, M$. That way we have both ψ_1^k and ψ_2^k , from which we can calculate ρ_k . Images can then be produced in .png format for each file using plotting libraries such as matplotlib (a python module)[24]. The set can then be concatenated and processed into a movie using an external file program, for example using FFmpeg[39] in LINUX in order to produce a video file.

BIDIMENSIONAL BOUND STATES FOR CHARGED
POLAR NANOPARTICLES

2.1 Introduction

We consider a many atoms cluster which is trapped between two impenetrable surfaces such that the system is restricted to two dimensions. We assume that it is ionized and has a permanent electric dipole. We will tackle three objectives: 1) Present a plot based discussion of the eigenfunctions involved. 2) Study the role in the theoretical description involving a constant of motion, which is the quantum counterpart to the one discussed in [22] 3) Taking into account the work in [41], we seek the modelling of the cluster using a central potential that allows the electrons to come close to the set of atoms if they are energetic enough. It is a penetrable region that is described via Gaussian potential of finite height, that can be passed through by an electron with just enough energy.

The system has been widely studied in the literature, paying special attention to the case of a particle in a Coulomb potential with the addition of a dipole term. There are analytical solutions for this type of problems, but, frequently, most attention is paid to the loss of spherical symmetry. Reference [42] looks at the energy levels of an electron moving in a field produced by two fixed charges $\pm e$, that are a distance R apart. They separated the equation in elliptical coordinates. They obtained two transcendental coupled equations and calculated the energies numerically. Their magnitude became less significant as R decreased. They also applied their results to the topic of lithium-boron embedded in silica and also to color centers in alkali halides. In [15], a study is carried out for the bound states of a system that consisted of a charged particle moving in an electric field. He showed that when the system was either a hard sphere or a finite dipole, the existence of the bound states depends solely on the reduced dipole moment $K = \frac{2M}{\hbar^2}eD$. They also found that the resulting behavior could be characterized by two different types of conducts: one where bound states can exist and another where they do not. One of their observations, which is of interest in this work, is that their results are valid for any repulsive potential at short distances that takes the form of a dipole potential in large distances. In [40] they studied the same problem using a variational method where they separated the equation in elliptic-parabolic coordinates. They found a minimum dipole moment $D_{min} = 0.6393$ such that for any $D < D_{min}$ there are no bound states. They successfully compared their results with those of Wallis et. al.[42] and plotted the contours of equiprobability on the plan of symmetry of the system. The reference [19] entreats a model where an electron moves in a field generated by a finite electric dipole. His Hamiltonian in atomic units was $H = -\frac{1}{2}\nabla^2 - \frac{q}{r} + \frac{q}{r^2}$. He interpreted the first two terms as an unperturbed Hamiltonian in order to build a trial wave function using the eigenfunctions of the hydrogen atom in a perturbation method. He used the variational method to calculate the ground state energy for a range of values of D . In [23], the authors studied a similar problem of an electron moving in the field of a finite dipole with a strong magnetic field. It was not until 2002 that exact solutions are obtained using analytic methods, though only for the case of point masses and, at most, with an added finite dipole. Reference [14] is concerned with the radial part of the problem, where it was found that its solutions are Bessel and Neuman functions. Reference [27] studies the three dimensional problem with a Coulomb potential plus three added potentials of the form: $\frac{a_j}{x_j^2}$, $j = 1, 2, 3$, where every a_j is different. They analyzed the problem using group theory paying attention to the system's symmetries and calculated its bound states.

They also used series of Legendre polynomials to write the radial equation's solutions and Jacobi polynomials for the angular part. The subject of the existence of a minimum electric dipole, necessary for the presence of bound states, was retaken by [13], who show that, for the cases of one and two dimensions, there is no such minimum dipole, and there are bound states in spite of the absence from a Coulomb potential. Citation [18] confirms the results obtained by Connolly and Griffiths so that, for two dimensions, there is at least one bound state.

Considering the results obtained above, we seek to develop a more realistic study in this work, where we model the behavior of an electron around a positively charged nanoparticle and a permanent electric dipole. We assume that the system is restricted to two dimensions and we do not use a point mass. We intend to discuss the topic, emphasizing the physics of the problem and recognizing the role played by the constant of motion mentioned paragraphs above. The physical states will be classified using two quantum numbers. We will plot a number of eigenfunctions from the angular part and the same amount for the radial part. We will also calculate Einstein's A coefficients.

2.2 Physical system

The system consists of a model where the presence of a nanoparticle in bidimensional space is represented as a penetrable circular region that prevents the flow of electrons. It is understood that it is possible to cross it if the electron has enough energy. Thus it will be modeled using a Gaussian potential $V_g(\vec{r})$ with finite height and width. The motivation of this work is to find out whether the electron can be captured by the nanoparticle in such a way that a sort of nano-atom emerges.

The Gaussian potential is of the form:

$$V_g(r) = Be^{-\left(\frac{r}{\sigma}\right)^2}, \quad (2.1)$$

where σ allows us to set the radius of the nanoparticle we seek to model. If the nanoparticle is ionized and has an intrinsic dipole moment, the potential energy is of the form

$$V_{nan}(|r - r_0|) = k_c \frac{qQ}{|\vec{r} - \vec{r}_0|} + k_c \frac{qD \cos(\theta)}{|\vec{r} - \vec{r}_0|^2}, \quad (2.2)$$

with \vec{r} and r_0 in vector notation; where $k_c = \frac{1}{4\pi\epsilon_0}$ is Coulomb's constant, Q is the electric charge of the nanostructure, and D is the dipole moment. Therefore the potential of the ionized nanostructure with an intrinsic dipole moment is

$$U(\vec{r}) = V_{nan}(\vec{r}) + V_g(r) \quad (2.3)$$

Schrödinger's equation is of the form:

$$-\frac{\hbar^2}{2m} \nabla^2 \psi(r, \theta) + \left[k_c \frac{qQ}{|\vec{r} - \vec{r}_0|} + k_c \frac{qD \cos(\theta)}{|\vec{r} - \vec{r}_0|^2} \right] \psi(r, \theta) = E\psi(r, \theta). \quad (2.4)$$

The equation is separable if $\vec{r}_0 = 0$. Using the polar coordinates

$$x = r \cos(\theta), \quad y = r \sin(\theta), \quad (2.5)$$

the Laplacian operator is of the form

$$\nabla^2 = \frac{\partial^2}{\partial r^2} + \frac{1}{r} \frac{\partial}{\partial r} + \frac{1}{r^2} \frac{\partial^2}{\partial \theta^2} = \nabla_r^2 + \frac{1}{r^2} \nabla_\theta^2, \quad (2.6)$$

with

$$\nabla_r^2 = \frac{\partial^2}{\partial r^2} + \frac{1}{r} \frac{\partial}{\partial r}, \quad \nabla_\theta^2 = \frac{\partial^2}{\partial \theta^2}. \quad (2.7)$$

and

$$U(r) = B e^{-\left(\frac{r}{\sigma}\right)^2} + k_c \frac{qQ}{r}, \quad U(\theta) = D \cos(\theta). \quad (2.8)$$

The potential can be rewritten as

$$U(\vec{r}) = U(r) + \frac{k_c}{r^2} qD \cos(\theta), \quad (2.9)$$

and we can write (2.4) as follows:

$$-\frac{\hbar^2}{2m} \left[\nabla_r^2 + \frac{1}{r^2} \nabla_\theta^2 \right] \psi(r, \theta) + \left[U(r) + \frac{k_c}{r^2} qD \cos(\theta) \right] \psi(r, \theta) = E \psi(r, \theta). \quad (2.10)$$

It is evident from (2.10) that the Hamiltonian can be expressed as:

$$\hat{H} = -\frac{\hbar^2}{2m} \nabla_r^2 + U(r) + \frac{1}{2mr^2} \hat{\beta}_\theta, \quad (2.11)$$

where

$$\hat{\beta}_\theta = -\hbar^2 \nabla_\theta^2 + 2mk_c qD \cos(\theta) \quad (2.12)$$

Where it can be demonstrated that $[\hat{\beta}_\theta, \hat{H}] = 0$, so that $\hat{\beta}_\theta$ represents a motion integral with a corresponding quantum number to classify the physical states of the system. There is no conservation of angular momentum but the term proportional to $\cos(\theta)$ in equation (2.12) compensates for it, leading to an integral of motion that we develop using a process of non-dimensionalization.

2.3 Non-dimensionalized equation

In order to remove dimensions from the equation we introduce a scale shift: $\vec{r} = \alpha \vec{\eta}$ with \vec{r} measured in meters and η being non-dimensional. The constant α will be selected later. The Laplacian is modified as follows:

$$\nabla_{\vec{r}}^2 = \frac{1}{\alpha^2} \nabla_{\vec{\eta}}^2, \quad (2.13)$$

so that the Schrödinger equation takes the form

$$\nabla_{\vec{\eta}}^2 \psi + \frac{2m\alpha^2}{\hbar^2} [E - qU(\vec{\eta})] \psi = 0. \quad (2.14)$$

Making it so that $\alpha = a_0$, where $a_0 = 5.29177210903(80) \times 10^{-11} m$ is the Bohr radius; the second term is:

$$\frac{2m\alpha^2}{\hbar^2} = \frac{2h^2}{k_c m e^4} = \frac{1}{E_1} \quad (2.15)$$

Where E_1 is the ground state of the energy spectrum of a hydrogen atom: $E_n = -\frac{E_1}{n^2}$. As is known, the value is $13.6eV$. Therefore, we can write (2.14) as:

$$\nabla_{\vec{\eta}}^2 \psi + \left[\frac{E}{|E_1|} - \frac{qU(\vec{\eta})}{|E_1|} \right] \psi = 0. \quad (2.16)$$

Where $\epsilon \equiv \frac{E}{|E_1|}$ is the energy as measured in Rydbergs, such that:

$$U(\eta) \equiv \frac{qU(\vec{\eta})}{|E_1|} = \frac{q}{|E_1|} \left\{ k_c \frac{Q}{\eta} + k_c \frac{D \cos(\theta)}{\eta^2} + B e^{-\left(\frac{\eta}{\sigma}\right)^2} \right\}. \quad (2.17)$$

In order to study the possible capture of an electron we take: $q = -e$. Making it so $Q = Ze$, where Z is the number of excess protons due to the nanostructure being ionized. The first term is:

$$U(\eta) = \frac{q}{|E_1|} k_c \frac{Q}{\eta} = -\frac{2Z}{\eta}, \quad (2.18)$$

and the second term is:

$$U_2(\eta) = \frac{q}{|E_1|} k_c \frac{D \cos(\theta)}{\eta^2} = \frac{2D \cos(\theta)}{a_0 e \eta^2}$$

The dipole unit at atomic scales will be the Debye: $Debye = 3.33564 \times 10^{-30} Cm$. If p is the electric dipole measured in Debyes, $p = \frac{1 \text{ Debye}}{3.33564 \times 10^{-30} Cm}$, such that $D = p \times (3.33564 \times 10^{-30} Cm)$. The factor multiplying $\cos(\theta)$ is $\frac{2D}{a_0 e} = p \times (0.78686)$. Denoting $g = 0.78686$, it results that:

$$U_2(\vec{\eta}) = g \frac{p \cos(\theta)}{\eta^2}. \quad (2.19)$$

For the third term we consider $\sigma = a_0 \sigma_\eta$ and define $A = \frac{eB}{|E_1|}$, so that the resulting magnitude of the Gaussian function is given in Rydbergs from here on out. It results that:

$$U_3(\vec{\eta}) = \frac{eB}{|E_1|} e^{-\left(\frac{\eta}{\sigma}\right)^2} = A e^{-\left(\frac{\eta}{\sigma_\eta}\right)^2} \quad (2.20)$$

To close, the potential has a final form of:

$$U(\eta) = -\frac{2Z}{\eta} + g \frac{p \cos(\theta)}{\eta^2} + A e^{-\left(\frac{\eta}{\sigma_\eta}\right)^2}. \quad (2.21)$$

Therefore, the reduced representation of the Schrödinger equation is

$$\nabla_{\vec{\eta}}^2 + \{\epsilon - U(\vec{\eta})\} \psi = 0. \quad (2.22)$$

2.4 Separation of variables

The potential $U(\eta)$ is expressed as the sum of a central potential term plus the dipole moment one. It is defined as:

$$U_\eta = -\frac{2Z}{\eta} + A e^{-\left(\frac{\eta}{\sigma_\eta}\right)^2} ; \quad U_\theta = gp \cos(\theta) \quad (2.23)$$

Denoting $\nabla_\eta^2 = \frac{\partial^2}{\partial \eta^2} + \frac{1}{\eta} \frac{\partial}{\partial \eta}$, and $\nabla_\theta^2 = \frac{\partial^2}{\partial \theta^2}$ so that the Schrödinger equation can be written as

$$\left[\nabla_\eta^2 + \frac{1}{\eta^2} \nabla_\theta^2 \right] \psi + \left\{ \epsilon - U_\eta - \frac{1}{\eta^2} U_\theta \right\} \psi = 0$$

We propose a solution of the form $\psi(\eta, \theta) = R(\eta)\Theta(\theta)$, and carrying out the standard calculation procedure for separation of variables yields two equations. The radial equation is

$$\left(\frac{\partial^2}{\partial \eta^2} + \frac{1}{\eta} \frac{\partial}{\partial \eta} + \epsilon - U_\eta - \frac{\lambda}{\eta^2} \right) R(\eta) = 0, \quad (2.24)$$

and the angular equation is

$$\left(-\frac{d^2}{d\theta^2} + gp \cos(\theta) - \lambda \right) \Theta(\theta) = 0, \quad (2.25)$$

which is the Mathieu equation [12]. Looking at (2.25) it is clear that it is an eigenvalue equation of the form:

$$\hat{B}\Theta(\theta) = \hbar^2 \lambda \Theta(\theta) \quad (2.26)$$

Where the operator is given by (2.12), so that the constant of motion that yields the quantum number λ is

$$\hat{B} = -\hbar^2 \frac{d^2}{d\theta^2} + \hbar^2 gp \cos(\theta). \quad (2.27)$$

The radial equation can be manipulated so that it takes a form that is similar to that of the Schrödinger equation in one dimension. We propose $R(\eta) = \frac{u(\eta)}{\sqrt{\eta}}$ so as to obtain

$$u'' + \left(\epsilon - U_\eta - \frac{\lambda - \frac{1}{4}}{\eta^2} \right) u = 0, \quad (2.28)$$

with an effective potential

$$U_{ef}(\eta) = -\frac{2Z}{\eta} + A e^{-\frac{\eta^2}{\sigma_\eta^2}} + \frac{\lambda - \frac{1}{4}}{\eta^2}. \quad (2.29)$$

It should be noted that λ appears in the centrifugal potential and is analogous to the angular momentum, where we will concentrate our study when $\lambda > 0$. The reasoning behind it is as follows: although λ is valued in the real numbers, its presence in the potential leads to an increasing in depth through the U_{ef} term as the values of λ become more negative, which is physically unacceptable.

The procedure followed in this work consists in solving the angular part in order to obtain both the eigenvalues λ and eigenfunctions $\Theta(\theta)$ with the periodic condition $\Theta(\theta) = \Theta(\theta + 2\pi)$. Afterwards, we numerically solve the radial equation in order to obtain the eigenfunctions $R_\eta(\eta)$, where n counts the number of nodes, and, since it has the same form as the Schrödinger equation, it has the same properties, in such a way that the resultant energies for each λ , can be organized in a crescent manner to match number of nodes n . In short, we have two quantum numbers: (m, n) , where the first numbers the eigenvalues of the Mathieu equation belonging to periodic solutions and the second numbers the nodes. The solutions will be denoted as Θ_m and R_n^m . The energies will depend on said quantum numbers and will be referred to as ϵ_{mn} .

2.5 Matthieu equation and its solutions

Although the system under consideration is idealized, we can address a case where an atom cluster adheres to a surface, where we impose constriction in the direction normal to the surface. Cluster size can be as large as several water molecules, for example. In order to choose values of the dipole moment, we pick a nanostructure formed by three molecules of gallium arsenide (GaAs). As has been reported by Karaminis et. al. [26], the clusters $(GaAs)_n$ with $n = 3, 4, 5$, present a variety of atomic arrays with differently valued dipole moments. In particular, when $n = 3$, in symmetry with C_s , they find that $p = 0.2589 D$. In this case $q = 4gp = 0.8147872$, where the eigenvector is $a = 4\lambda$. Using the change of variable $\theta = 2\gamma$ and $0 \leq \gamma \leq \pi$, the equation takes the form

$$\left(-\frac{d^2}{d\gamma^2} + 4gp \cos(2\gamma) - 4\lambda\right) \Theta(\gamma) = 0 \quad (2.30)$$

The usual notation for the Mathieu equation is:

$$\left(-\frac{d^2}{dz^2} + q \cos(2z) - a\right) y(z) = 0, \quad (2.31)$$

where the electric dipole moment determines q and a is related to λ . The presence of a periodic coefficient means that the expression fulfills Floquet's theorem, which establishes that there will always be an associated solution where the following relation is true:

$$y(z + \pi) = \sigma y(z) \quad (2.32)$$

Where σ is a constant that depends on the values of q and a . As a corollary of the theorem, it can be demonstrated that, for the Mathieu equation, there will always exist one solution of the form:

$$y(z) = e^{i\nu z} \phi(z), \quad (2.33)$$

where $\phi(z)$ is always of period π , and where ν is referred to as either periodicity factor or characteristic exponent.

The solutions with greater physical interest are those of period 2π or π and are named basically periodic functions. For these kinds of solutions, if a and q are real valued, and ν is any characteristic exponent, then ν will necessarily be an integer. Also, if q is real, a will be also, so that way λ can be a physical quantity.

For our problem, we need that $\Theta(\gamma) = \Theta(\gamma + \pi)$, where ν has to be an integer [12]. Also, the only expression that showcases a physically significant conduct is the even function for the case when $q \rightarrow 0$. This specific case will be the only one that we will be considering moving forward.

The eigenfunctions satisfy the orthonormalization relation

$$\int_0^\pi \Theta_{a_1}(\gamma) \Theta_{a_2}(\gamma) d\gamma = \frac{1}{\pi} \delta_{a_1, a_2} \quad (2.34)$$

Thus, the set of eigenfunctions $\{\Theta_a\}$ generates every solution for the angular part of the problem.

In physical terms, the system has a dipole moment p , thus, we want to explore how changes to the critical exponent ν affect the eigenvalue a 's magnitude.

We consider the electric dipole of a $(GaAs)_3$ cluster with C_s symmetry as iconic case. Its electric dipole moment is $p = 0.2589$.

In order to study the angular part we used the software Mathematica to calculate the solutions. Results are shown in Figure 2.1.

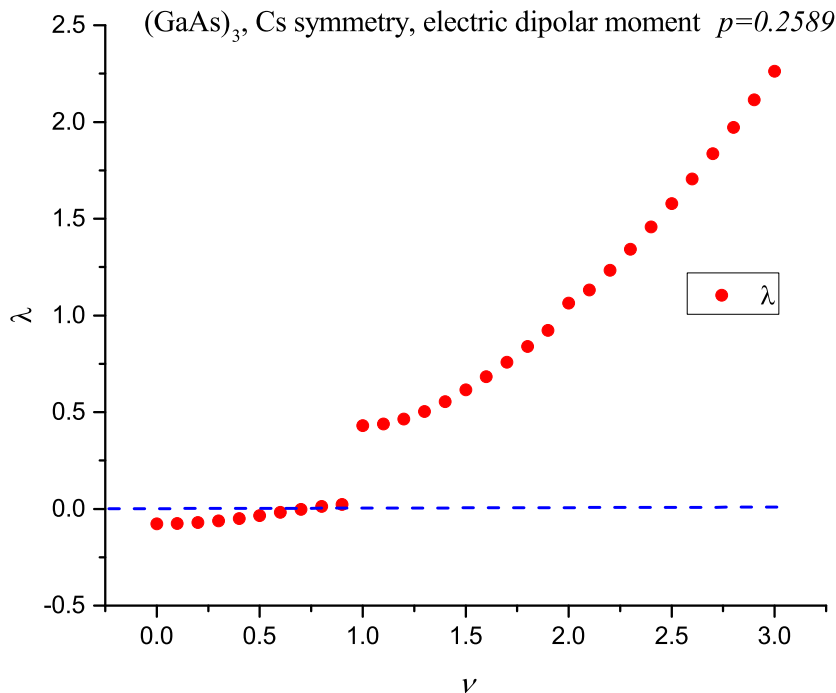


Figure 2.1: λ values for different characteristic exponents ν . There is a discontinuity close to $\nu = 1.0$. In order to obtain angular functions of period π , ν must be an integer.

From the plot, it is clear that, for $\nu < 0.8$, the values for λ are negative. There is also a discontinuity when $\nu \rightarrow 1.0$.

As we previously mentioned, we need that $\Theta(\gamma) = \Theta(\gamma + 2\pi)$ for our problem, therefore, ν must be an integer. For the case when p is the electric dipole moment of the $(GaAs)_3$ cluster, we make the critical exponent vary across $\nu = \{1.0, 2.0, 3.0, 4.0\}$. This set of magnitudes produce the following values for a and $\lambda = \frac{1}{4}a$:

ν	a	λ
1.0	1.72326	0.430815
2.0	4.25544	1.06386
3.0	9.0501	2.26253
4.0	16.0224	4.00559

Table 2.1: Eigenvalues λ for every characteristic exponent. They must be non-negative so that the centrifugal potential responds in a manner that is similar to when the dipole is zero.

In order to study the angular part we used the software Mathematica to calculate the solutions. The eigenfunctions corresponding to the angular part and for each value of λ are shown in Figure 2.2.

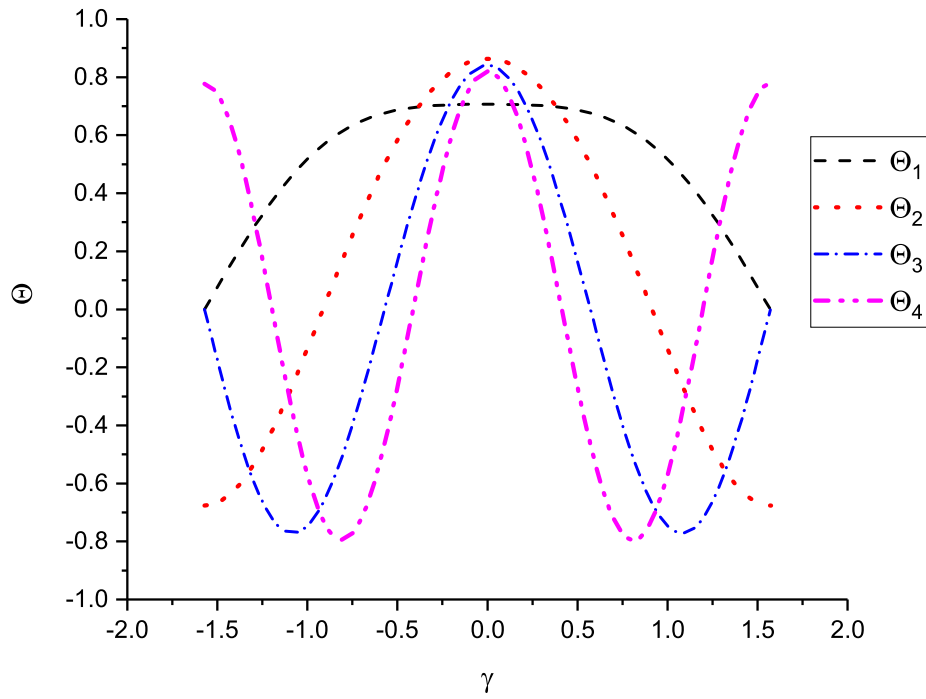


Figure 2.2: Angular functions for the first four characteristic exponents.

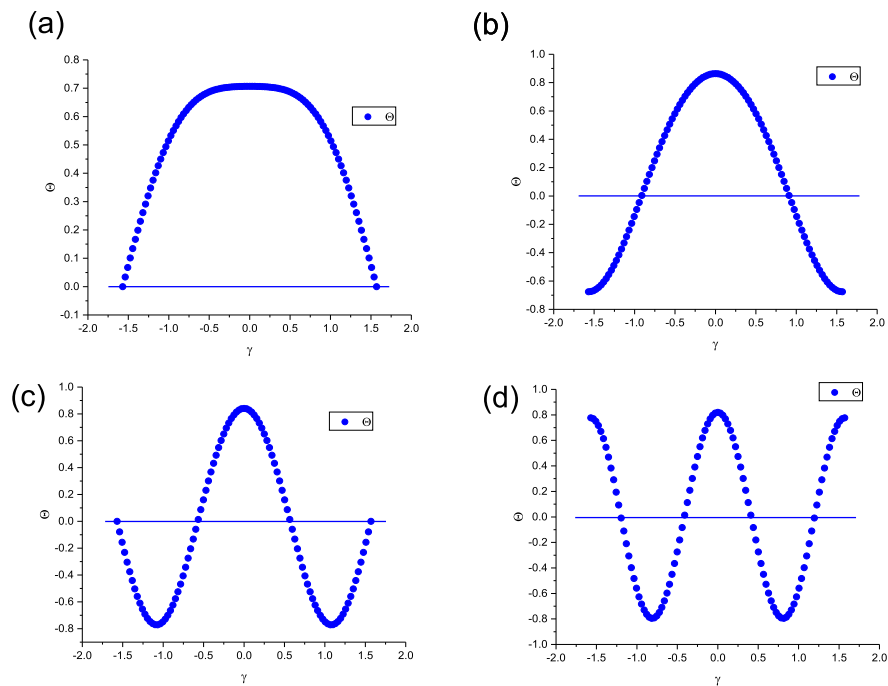


Figure 2.3: Probability amplitude. The values of ν and λ are given in table 2.1.

The probability amplitudes are shown separately in Figure 2.3.

The eigenfunction Θ_1 shows that the probability density has only one preferred direction, with a maximum at $\gamma = 0$. On the other hand, Θ_2 presents two preferential directions: the first being $\gamma = 0$ and the second being in the opposite direction but less pronounced. The state Θ_3 has a maximum in $\gamma = 0$ and two local probability maxima in $\gamma = \pm 1.06814$ which corresponds approximately to $\theta = \pm 122$ degrees. Finally, Θ_4 distributes its probability among four orthogonal maxima.

2.6 Radial equation

The effective potential is given by

$$U_{eff}(\eta) = -\frac{2Z}{\eta} + Ae^{-\frac{\eta^2}{\sigma^2}} + \frac{\lambda - \frac{1}{4}}{\eta^2}, \quad (2.35)$$

so that we have a set of energy values for each λ .

We have taken $A = 10$, which physically means that an electron with energy of 136 eV can pass through the nanostructure. We have also taken $\sigma = 7$, which allows us to represent a region whose presence is progressively registered by the electron within half a nanometer of its center.

A plot of the values $\lambda = 0.430815$ and $\lambda = 4.00559$ is shown in Figure 3.4.

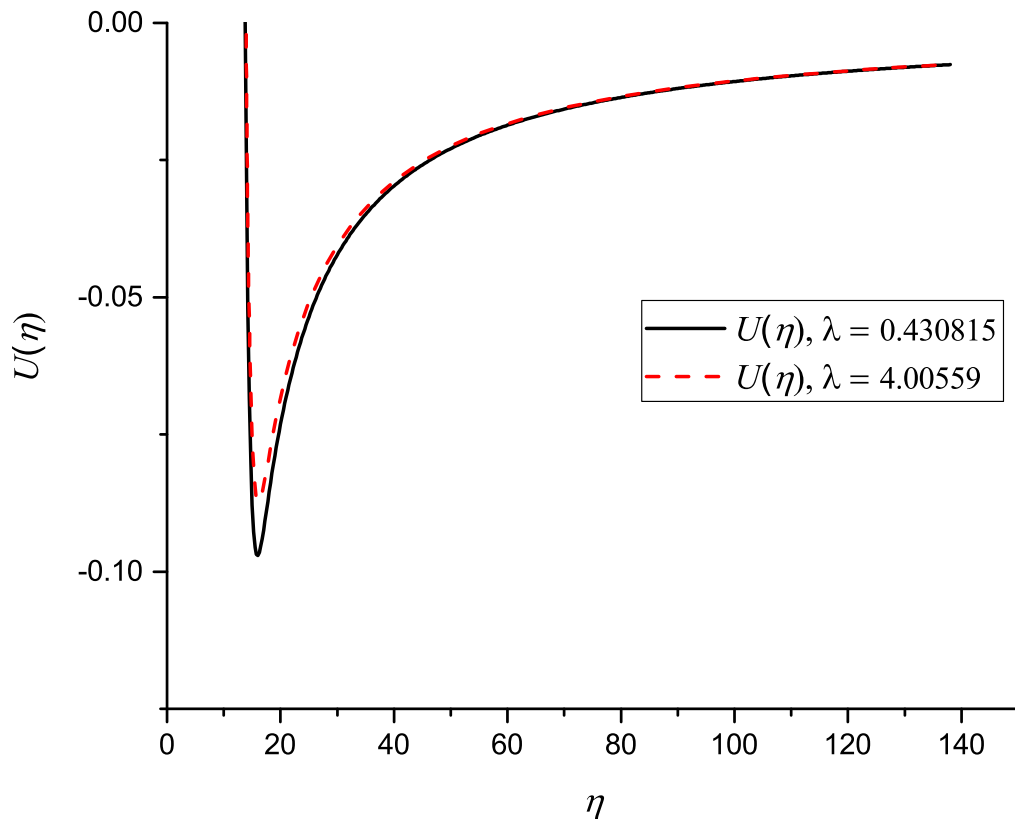


Figure 2.4: Potential for distinct values of λ . An eigenvalue for the constant of motion acts like the angular momentum, as is seen in the case when the electric dipole moment is zero.

The potential is used as model of the nanostructure as a barrier that shows energy minimums at almost a nanometer of distance. Its shape makes the model interesting given the existence of bound states close to a nanometer from the center, suggesting the potential plays an active role in the nucleation process, so long as it is ionized and has a permanent dipole moment.

Equation (2.28) was solved numerically using the shooting method. Solutions have a typical form, which shows up for the value $\lambda = 0.4308$. We obtained a ground state and three excited states whose properties are as expected. That is to say: the number of nodes corresponds either to the ground or excited states. We also find that there are many bound states for $n \geq 4$, but their energies are so close between them that the shooting method struggles to detect them. The plot for the first three energy levels is shown in Figure 3.5.

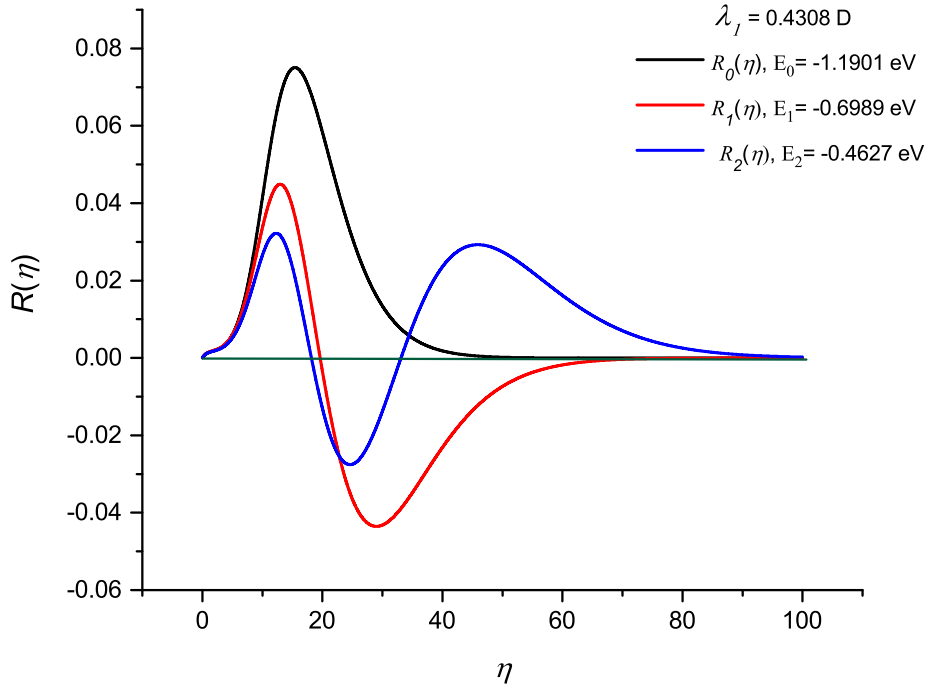


Figure 2.5: Radial component of the probability amplitude for the ground state and three excited states. The quantum numbers $n = 0, 1, 2, 3$, equals the number of nodes.

There is similar conduct for $\lambda_2, \lambda_3, \lambda_4$.

Physical states are classified via the two available quantum numbers when enumerating $m = 1, 2, 3, 4$ for the obtained eigenvalues of λ , and $n = 1, 2, 3$ for the nodes of each solution belonging to the radial function. They are denoted as $|mn\rangle$ and its energies as E_{mn} .

The energy eigenvalues are as shown in table 2.2.

	$n = 0$ (eV)	$n = 1$ (eV)	$n = 2$ (eV)	$n = 3$ (eV)
$\lambda_1, m = 1$	-1.19058	-0.699242	-0.462896	-0.329456
$\lambda_2, m = 2$	-1.158	-0.682652	-0.453439	-0.323594
$\lambda_3, m = 3$	-1.09886	-0.652845	-0.436463	-0.313057
$\lambda_4, m = 4$	-1.01839	-0.612728	-0.413586	-0.298805

Table 2.2: Energies of the ground state and for the first three bound states, where m enumerates the eigenvalue λ . For each of these, there is a potential and, in return, a set of radial solutions with its respective energy.

2.7 Transition rates (A-coefficients)

Angular momentum must be conserved in a joint setup of an atomic system plus electromagnetic radiation. This means that emission or absorption of a photon that transports angular momentum $\pm h$, implies the change νh in the atomic system. In the case of spherically symmetric systems, this translates into selection rules that can be calculated via matrix elements. On the other hand, in the system we are treating in this work, the conservation law is expressed as $[\hat{B}, \hat{H}] = 0$, where \hat{B} is given by equation (2.27). Consequently, every matrix element must be calculated. The transitions between states sharing same particular λ are not considered because the variation of $4gp \cos(\theta)$ produces values smaller than one, and a rate of change larger or equal to \hbar is not possible.

The Einstein coefficient $A_{m'n',mn}$ between pairs of physical states $m'n'$ and mn is given as such

$$A_{m'n',mn} = \frac{e^2(2\pi\nu_{m'n',mn})^3}{3\pi\epsilon_0\hbar c^3} |\langle m'n' | \vec{r} | mn \rangle|^2$$

We calculated 96 coefficients A, and selected the 18 with highest magnitude in order to know the most intense spectral lines. The results are presented in table 2.3 along with its associated wavelengths.

Coefficient A ($\frac{1}{s}$)	Wavelength
$A_{12,32} = 9.02614 \times 10^{12}$	2.67845 <i>microns</i>
$A_{12,42} = 6.69492 \times 10^{11}$	2.67845 <i>microns</i>
$A_{21,41} = 6.69492 \times 10^9$	17.7313 <i>microns</i>
$A_{22,42} = 2.76650 \times 10^9$	31.1099 <i>microns</i>
$A_{11,41} = 2.65975 \times 10^9$	14.3312 <i>microns</i>
$A_{11,31} = 2.15226 \times 10^9$	26.7227 <i>microns</i>
$A_{23,43} = 1.25145 \times 10^9$	50.0153 <i>microns</i>
$A_{31,41} = 5.36648 \times 10^8$	30.9057 <i>microns</i>
$A_{13,43} = 4.91928 \times 10^8$	40.4504 <i>microns</i>
$A_{13,33} = 4.11284 \times 10^8$	75.6038 <i>microns</i>
$A_{32,42} = 2.24076 \times 10^8$	54.1960 <i>microns</i>
$A_{11,21} = 1.21213 \times 10^8$	74.7368 <i>microns</i>
$A_{21,31} = 1.01924 \times 10^8$	41.5955 <i>microns</i>
$A_{33,43} = 1.01727 \times 10^8$	86.9961 <i>microns</i>
$A_{12,22} = 5.11606 \times 10^7$	131.111 <i>microns</i>
$A_{22,32} = 4.27161 \times 10^7$	73.0324 <i>microns</i>
$A_{13,23} = 2.35310 \times 10^7$	211.517 <i>microns</i>
$A_{23,33} = 1.95293 \times 10^7$	117.66 <i>microns</i>

Table 2.3: The measured Einstein coefficients with the most significant magnitude. All frequencies are located in the infrared spectrum.

Where the most intense spectral lines disperse from near infrared, at 2.67845 microns, up to 211.517 microns which is at the far end of the infrared spectrum and all its A coefficients are bigger than, say, the one corresponding to the transition from state $3s$ to $2p$ of the hydrogen atom, such that half-lives of the system under study are shorter than in the cited example.

2.8 Conclusions

In this chapter, we modeled the motion of an electron in the vicinity of an ionized nanostructure with a permanent electric dipole. Although we worked the example of a $(GaAs)_3$ cluster with C_s symmetry, this approach can be generalized to a nanoparticle of arbitrary size. We non-dimensionalized Schrödinger's equation and separated it in polar coordinates, and we showed that there exists an integral of motion in which the angular momentum is compensated via a term that is proportional to $\cos(\theta)$. The eigenfunctions can be classified via two quantum numbers: the eigenvalue λ and the number of nodes in the radial component of the solution. In this case, the eigenvalue present in the effective potential is an analogue to that of an angular momentum in problems with spherical symmetry. The energy levels can be enumerated by them.

We restricted our study to the values $\nu = 1, 2, 3, 4$ of the characteristic exponent with its respective values for λ . For each of these, we obtained the radial solutions and their corresponding eigenfunctions using the shooting method, which is very useful but it comes at a cost in the resolution, in terms of detecting energy levels of bound states that are too close by, as they approach zero. We also made a table of 16 energy levels, and calculated 96 transition rates in order to evaluate Einstein's $A_{n'm',nm}$ coefficient, and present the 18 highest ones, together with their corresponding wavelengths, all of them located in the infrared part of the electromagnetic spectrum.

BEHAVIOR OF AN ELECTRON IN THE VICINITY OF A
TRIDIMENSIONAL CHARGED POLAR
NANOPARTICLE THROUGH A CLASSICAL AND
QUANTUM CONSTANT OF MOTION

3.1 Introduction

In this chapter, we study the conduct of an electron in the vicinity of a nanostructure formed by multiple atoms. We assume that the nanostructure is ionized and that it has a permanent electric dipole. It is a generalization of the bidimensional system solved previously [9]. Similar cases to what we worked here have been widely studied in the literature, paying special attention to the case of a point particle with a Coulomb potential plus a dipole term. We calculate a constant of motion which is a generalization of the one published by Gutierrez et al [22]. We first study the motion from a classical standpoint and then the approach is generalized to quantum mechanics. This is a problem that has been tackled analytically before, but without taking full advantage of the constant of motion discussed in this chapter. The system has been studied when the potential is solely dipolar in nature, when a magnetic field is added, and also after adding a Coulomb potential. The studies in references [42, 15, 40, 19, 23, 14, 27, 13, 18] encompass both the classical Newtonian regime as well as the relativistic quantum one.

Inspired by the work of R. Van Zon [41], we seek to develop a more realistic model in which we study an electron in the vicinity of a positively charged nanoparticle and a permanent electric dipole but without recurring to a point mass. Instead we make use of a Gaussian potential that includes the rejection stemming from the electron cloud representing the nanostructure over the bound electron. In the study of the Newtonian classical regime we obtain the conditions under which there can be bounded orbits that are stable, which allows us to look for bound states in the non-relativistic quantum system. Its physical states are classified using three quantum numbers and we explore the difference between the eigenfunctions as well as the particular case where spherical symmetry is present due to the electric dipole being absent. We plot some of the eigenfunctions for the angular and radial solutions. We present the energies of the ground state as well as the first and second excited states. Their magnitudes are compared with the thermal energy at 300K (2.5852×10^{-2} eV) to show that the electron is bound to the extent that it can resist perturbations from thermal agitation. As consequence, we obtain the wavelengths of the electromagnetic energy necessary for the structure to lose the electron that has been caught and we propose that these can be detected in gaseous form in nature if subjected to frequencies in the long wavelength infrared and the far infrared range.

3.2 Classical approach

In this section, we show that the constant of motion obtained in [22] for the purely dipole potential $V(\vec{r}) = \frac{\vec{d} \cdot \vec{r}}{4\pi\epsilon_0 r^2}$ is also valid if one adds the Coulomb interaction plus an arbitrary central potential. In this case \vec{d} is the dipole moment and \vec{r} the position of the charged particle, where the coordinate system is placed in the center of mass of the nanostructure. We obtain the conditions for which there can be stable and bounded orbits, we will find an expression for the depth of the interacting potential and also analyze the motion in the radial coordinate r .

The constant of motion will be obtained via two different approaches: the Hamilton-Jacobi equation and a purely Newtonian one.

3.2.1 Calculation of the constant of motion from the Hamilton-Jacobi equation.

We use spherical coordinates (r, θ, ϕ) , where the z axis is aligned with the dipole moment \vec{d} . The potential energy of the charged particle is

$$V(r, \theta) = \frac{\gamma}{r} + \frac{k'}{r^2} \cos(\theta) + V_g(r), \quad (3.1)$$

where $\gamma \equiv \frac{qQ}{4\pi\epsilon_0}$, $k' = \frac{qd}{4\pi\epsilon_0}$ and $V_g(r)$ is a short range central potential used to model the impossibility of an electron to pass through the nanostructure so long as its energy is not large enough. The origin of our coordinate system is placed at the point occupied by the charge Q and the point-like electric dipole. Denoting Δ_0 as the dimensions of the nanostructure one imposes the condition that $V_g(r)|_{r=\Delta_0} \simeq 0$ and $\frac{dV_g(r)}{dr}|_{r=\Delta_0} \simeq 0$.

Note that (3.1) is not a central potential, so that the angular momentum is not conserved. The expression for the energy depends on two variables: r and θ . It does not represent motion on a plane and the standard techniques found in text books cannot be used to address the question of whether bounded and stable orbits exist.

The Hamiltonian function for a particle of mass m and charge q is

$$H = \frac{1}{2m} \left(p_r^2 + \frac{p_\theta^2}{r^2} + \frac{p_\phi^2}{r^2 \sin^2(\theta)} \right) + V(r, \theta) \quad (3.2)$$

We take the Hamilton-Jacobi equation as our starting point for the principal function S :

$$H \left(r, \theta, \phi, \frac{\partial S}{\partial r}, \frac{\partial S}{\partial \theta}, \frac{\partial S}{\partial \phi}, t \right) + \frac{\partial S}{\partial t} = 0. \quad (3.3)$$

For conservative systems in which H does not depend explicitly on t , Hamilton's principal function S takes the form:

$$S(r, \theta, \phi, t) = S_0(r, \theta, \phi) - Et, \quad (3.4)$$

where E is the total constant energy and S_0 is the characteristic function, or abbreviated action, that satisfies the Hamilton-Jacobi equation:

$$H \left(r, \theta, \phi, \frac{\partial S_0}{\partial r}, \frac{\partial S_0}{\partial \theta}, \frac{\partial S_0}{\partial \phi} \right) = E. \quad (3.5)$$

Thus for our problem, the modified Hamilton-Jacobi equation is

$$\frac{1}{2m} \left[\left(\frac{\partial S_0}{\partial r} \right)^2 + \frac{1}{r^2} \left(\frac{\partial S_0}{\partial \theta} \right)^2 + \frac{1}{r^2 \sin^2(\theta)} \left(\frac{\partial S_0}{\partial \phi} \right)^2 \right] + \frac{\gamma}{r} + \frac{k' \cos(\theta)}{r^2} + V_g(r) = E. \quad (3.6)$$

In this case, since ϕ is a cyclic coordinate, we look for the solution of (3.6) in the form

$$S_0(r, \theta, \phi) = P_\phi \phi + S_1(r) + S_2(\theta), \quad (3.7)$$

where P_ϕ is the canonical conjugate moment of ϕ and it is a constant. The form of equation (3.6) is similar to that of the time independent Schrödinger equation, that will be addressed later on.

From (3.7) it follows that $p_\phi = \left(\frac{\partial S_\phi}{\partial \phi}\right)$. Substituting (3.7) in (3.6), and separating variables, one obtains two ordinary differential equations:

$$\left(\frac{dS_2(\theta)}{d\theta}\right)^2 + 2mk' \cos(\theta) + \frac{p_\phi^2}{\sin^2(\theta)} = \beta, \quad (3.8)$$

$$\frac{1}{2m} \left(\frac{dS_1(r)}{dr}\right)^2 + \frac{\gamma}{r} + V_g(r) + \frac{\beta}{2mr^2} = E, \quad (3.9)$$

where β is a separation constant. The solutions are:

$$S_2(\theta) = \int \sqrt{\beta - 2mk' \cos(\theta) - \frac{p_\phi^2}{\sin^2(\theta)}} d\theta, \quad (3.10)$$

$$S_1(r) = \int \sqrt{2m \left[E - \frac{\gamma}{r} - V_g(r)\right] - \frac{\beta}{r^2}} dr, \quad (3.11)$$

Repeating the same procedure for (3.10) and (3.11) in (3.7), results in

$$\begin{aligned} S_0(r, \theta, \phi) = p_\phi \phi + \int \sqrt{\beta - 2mk' \cos(\theta) - \frac{p_\phi^2}{\sin^2(\theta)}} d\theta \\ + \int \sqrt{2m \left[E - \frac{\gamma}{r} - V_g(r)\right] - \frac{\beta}{r^2}} dr \end{aligned} \quad (3.12)$$

Plugging (3.12) in (3.4) one obtains

$$\begin{aligned} S = -Et + p_\phi \phi \\ + \int \sqrt{\beta - 2mk' \cos(\theta) - \frac{p_\phi^2}{\sin^2(\theta)}} d\theta \\ + \int \sqrt{2m \left[E - \frac{\gamma}{r} - V_g(r)\right] - \frac{\beta}{r^2}} dr. \end{aligned} \quad (3.13)$$

The expression is a complete integral of the Hamilton-Jacobi equation as given by (3.3), with E, p_ϕ, β as independent constants.

From (3.13) we obtain

$$p_\theta = \frac{\partial S}{\partial \theta} = \sqrt{\beta - 2mk' \cos(\theta) - \frac{p_\phi^2}{\sin^2(\theta)}} \quad (3.14)$$

From this expression one can calculate the value of β , which is the following function of the coordinates and generalized momenta:

$$\beta = \left(P_\theta^2 + \frac{p_\phi^2}{\sin^2(\theta)}\right) + 2mk' \cos(\theta) = L^2 + 2mk' \cos(\theta). \quad (3.15)$$

Which is a constant of motion and contains L^2 as one of its terms, which is the angular momentum. Accounting for three constants of motion, E, p_ϕ , and β , it is possible to analyze the physical system using similar techniques for central field problems found in academic textbooks.

From (3.13) we can obtain the generalized momentum p_r :

$$p_r = \frac{\partial S}{\partial r} = \sqrt{2m \left[E - \frac{\gamma}{r} - V_g(r) \right]} - \frac{\beta}{r^2}, \quad (3.16)$$

which will be useful in order to study the motion of the particle for the radial coordinate.

3.2.2 Calculating the constant of motion from a Newtonian approach

It is also possible to obtain the motion constant β via more elemental means. In this section we present a purely Newtonian way to arrive at expression (3.15). We follow closely the calculations carried out by Gutierrez et al [22].

We denote \vec{F} as the electric force of a charge Q , with dipole \vec{d} , acting on another charge q , the latter being the one whose classical motion we are interested in analyzing. The potential of the nanostructure is

$$u(r, \theta) = \frac{1}{4\pi\epsilon_0} \frac{Q}{r} + \frac{\vec{d} \cdot \vec{r}}{4\pi\epsilon_0 r^2} + u_g(r), \quad (3.17)$$

where $u_g(r) = \frac{1}{q} V_g(r)$ represents the nanostructure. The energy of the interaction between both charges is $V(r, \theta) = q u(r, \theta)$ and the force acting on the electron is $\vec{F}(r, \theta) = -q \nabla u(r, \theta)$. If r is of the order of Δ_0 , the potential $u_g(r)$ impresses a force upon the particle given by: $\vec{F}_g = -\nabla V_g(r) = -\frac{dV_g(r)}{dr} \hat{r}$.

One first calculates the torque acting upon the particle of charge q :

$$\vec{N} = \vec{r} \times \left[\frac{3q}{4\pi\epsilon_0} \frac{\vec{r} \cdot \vec{d}}{r^5} \vec{r} - \frac{q}{4\pi\epsilon_0} \frac{\vec{d}}{r^3} + \frac{q}{4\pi\epsilon_0} \frac{Q}{r^3} \vec{r} - \frac{dV_g(r)}{dr} \hat{r} \right], \quad (3.18)$$

Since $\vec{r} \times \vec{r} = 0$, the expression is reduced to

$$\vec{N} = -\frac{q}{4\pi\epsilon_0} \frac{\vec{r} \times \vec{d}}{r^3}, \quad (3.19)$$

so that $\vec{N} \cdot \vec{d} = 0$.

Therefore from the equation for the time evolution of the angular momentum \vec{L} ,

$$\vec{N} = \frac{d\vec{L}}{dt}, \quad (3.20)$$

it follows that the component \vec{L} in the direction of \vec{d} is constant.

Taking the interior product of \vec{L} with (3.19) produces

$$\vec{L} \cdot \frac{d\vec{L}}{dt} = \frac{1}{2} \frac{dL^2}{dt} = -\frac{q}{4\pi\epsilon_0 r^3} \vec{L} \cdot (\vec{r} \times \vec{d}). \quad (3.21)$$

Starting from the definition of angular momentum: $L^2 = (\vec{r} \times \vec{v}) \cdot (\vec{r} \times \vec{v})$, where \vec{v} is the particle's velocity. Using vector identities and rearranging terms, results in

$$\frac{dL^2}{dt} = -\frac{qm}{2\pi\epsilon_0}\vec{d}\cdot\left[\frac{1}{r}\frac{d\vec{r}}{dt}-\frac{\vec{r}}{r^2}\frac{dr}{dt}\right], \quad (3.22)$$

where the bracketed term is $\frac{d\hat{r}}{dt}$, so that the previous equation can be written as

$$\frac{dL^2}{dt} = -\frac{qm}{2\pi\epsilon_0}\vec{d}\cdot\frac{d\hat{r}}{dt}.$$

Since \vec{d} is a constant vector, $\frac{d\vec{d}}{dt} = 0$, one can add zero to write

$$\frac{dL^2}{dt} = -\frac{qm}{2\pi\epsilon_0}\frac{d(\vec{d}\cdot\hat{r})}{dt}. \quad (3.23)$$

Rearranging terms we obtain

$$\frac{d\left[L^2 + \frac{qm}{2\pi\epsilon_0}(\vec{d}\cdot\hat{r})\right]}{dt} = 0, \quad (3.24)$$

from where we can deduce the constant of motion as seen in (3.15):

$$\beta = L^2 + \frac{qm}{2\pi\epsilon_0}(\vec{d}\cdot\hat{r}) \quad (3.25)$$

3.2.3 Analysis of motion in the radial coordinate

Going from equation (3.16), it must be true that p_r must only be valued in the real numbers. If so, the following must also hold:

$$E \geq \frac{\gamma}{r} + V_g(r) + \frac{\beta}{2mr^2}. \quad (3.26)$$

Defining the effective potential

$$V(r)_{eff} = \frac{\gamma}{r} + \frac{\beta}{2mr^2} + V_g(r), \quad (3.27)$$

we can rewrite (3.26) as

$$E \geq V(r)_{eff} \quad (3.28)$$

We focus in the case when $\gamma < 0$, $\beta > 0$.

The condition $\left(\frac{dV_{eff}}{dr}\right)|_{r=r_c}$ defines a point where the potential reaches its minimum. For energies such that the following inequality holds: $V_{eff}(r_c) < E < 0$. It means that the radial coordinate of the particle is located at the interval $r_{min} \leq r \leq r_{max}$. In this case, motion is bound because the trajectory is contained within a region delimited by two spheres centered at the origin whose radii are r_{min} and r_{max} respectively.

To determine the value of the radial coordinate at the minimum (of the potential) we make use of the previously mentioned condition, expressed as: $\left.\frac{dU_g(r)}{dr}\right|_{r=\Delta_n} \simeq 0$; we calculate the derivative, equal to zero and we obtain the relation

$$r_c = -\frac{\beta}{\gamma m} = -\frac{4\pi\epsilon_0\beta}{qQm}, \quad (3.29)$$

and the minimum is

$$V_{eff}(r_c) = - \left(\frac{qQ}{4\pi\epsilon_0} \right)^2 \frac{m}{2\beta} \quad (3.30)$$

Classically, r_c grows linearly with β , and $V_{eff}(r_c)$ grows in the order of β^{-1} . These results will be useful in the quantum treatment of the same problem.

3.2.4 Analysis of motion of the angular coordinate

From equation (3.25) it results that $\beta \geq \frac{qmd}{2\pi\epsilon_0} \cos(\theta)$. Defining the function $f(\theta) = \frac{qmd}{2\pi\epsilon_0} \cos(\theta)$, and focusing on the case when $q < 0$, we get the following inequality:

$$f(\theta) \leq \beta. \quad (3.31)$$

Where equality for the rightmost term in expression (3.31) is obtained when the angle θ_1 is

$$\theta_1 = \arccos \left(\frac{2\pi\epsilon_0}{qmd} \beta \right), \quad (3.32)$$

which means the charge q can move in a range of $0 \leq \theta \leq \theta_1$.

3.3 Quantum approach

The system models a nanoparticle in space as a penetrable sphere that impedes the free access of electrons. It is understood that the particle can pass through the nanostructure only if it has enough energy. This is modeled through a potential $V_g(\vec{r})$ of finite height and width. We seek to study the properties of a bound electron in a way that a "nano atom" is generated through the interactions.

We model the nanostructure as a Gaussian potential that is then added to the Schrödinger equation:

$$V_g(\vec{r}) = Ae^{-\left(\frac{r}{\sigma}\right)^2}, \quad (3.33)$$

where σ is the parameter lets us set the radius of the nanoparticle we seek to model.

If the nanostructure is ionized and has intrinsic dipole moment, the potential is

$$V_{nan}(\vec{r}) = \frac{1}{4\pi\epsilon_0} \frac{qQ}{|\vec{r}|} + \frac{1}{4\pi\epsilon_0} \frac{qp \cos(\theta)}{|\vec{r}|^2}, \quad (3.34)$$

where Q is the electric charge of the nanostructure and p is the dipole moment. The potential of the ionized nanostructure with intrinsic dielectric dipole is

$$U(\vec{r}) = V_{nan} + V_g(\vec{r}). \quad (3.35)$$

The Schrödinger equation takes the following form:

$$-\frac{\hbar^2}{2m} \nabla^2 \psi(r, \theta) + \left[\frac{1}{4\pi\epsilon_0} \frac{qQ}{|\vec{r}|} + \frac{1}{4\pi\epsilon_0} \frac{qp \cos(\theta)}{|\vec{r}|^2} + Ae^{-\left(\frac{r}{\sigma}\right)^2} \right] \psi(r, \theta) = E\psi(r, \theta, \phi) \quad (3.36)$$

The Laplacian in spherical coordinates is

$$\nabla^2 = \nabla_r^2 + \frac{1}{r^2} \nabla_\Omega^2, \quad (3.37)$$

with

$$\nabla_r^2 = \frac{1}{r^2} \frac{\partial}{\partial r} \left(r^2 \frac{\partial}{\partial r} \right), \quad \nabla_\Omega^2 = \frac{1}{\sin^2(\theta)} \frac{\partial^2}{\partial \phi^2} + \frac{1}{\sin(\theta)} \frac{\partial}{\partial \theta} \left(\sin(\theta) \frac{\partial}{\partial \theta} \right). \quad (3.38)$$

Defining

$$U(r) = Ae^{-\left(\frac{r}{\sigma}\right)^2} + \frac{1}{4\pi\epsilon_0} \frac{qQ}{r^2}, \quad U(\theta) = p \cos(\theta), \quad (3.39)$$

so that the potential can be rewritten as

$$U(\vec{r}) = U(r) + \frac{1}{4\pi\epsilon_0} qp \cos(\theta). \quad (3.40)$$

We can write (3.36) as

$$-\frac{\hbar^2}{2m} \left[\nabla_r^2 + \frac{1}{r^2} \nabla_\Omega^2 \right] \psi(r, \theta) + \left[U(r) + \frac{1}{4\pi\epsilon_0} qp \cos(\theta) \right] \psi(r, \theta, \phi) = E\psi(r, \theta, \phi). \quad (3.41)$$

From equation(3.41), it is evident that the Hamiltonian can be expressed as follows:

$$\hat{H} = -\frac{\hbar^2}{2m} \nabla_r^2 + U(r) + \frac{1}{2mr^2} \hat{\beta}_\Omega, \quad (3.42)$$

where

$$\hat{\beta}_\Omega = -\hbar^2 \nabla_\Omega^2 + \frac{mqp}{2\pi\epsilon_0} \cos(\theta). \quad (3.43)$$

It is direct to demonstrate that $[\hat{\beta}_\Omega, \hat{H}] = 0$, so that $\hat{\beta}_\Omega$ is a constant of motion with a corresponding quantum number to classify the physical states of the system. The angular momentum is not conserved, but the term proportional to $\cos(\theta)$ compensates for it.

3.3.1 Non-dimensionalized equation

In order to non-dimensionalize the equation, we will introduce scale change: $\hat{r} = \alpha \vec{\eta}$, where \vec{r} is measured in meters and $\vec{\eta}$ has no units. The constant α will be selected ahead.

The Laplacian is modified as follows:

$$\nabla_{\hat{r}}^2 = \frac{1}{\alpha^2} \nabla_{\vec{\eta}}^2, \quad (3.44)$$

so that the Schrödinger equation is

$$\nabla_{\vec{\eta}}^2 \psi + \frac{2m\alpha^2}{\hbar^2} [E - qU(\vec{\eta})] \psi = 0. \quad (3.45)$$

If we set α to be equal to the Bohr radius, a_0 , the coefficient for the second term is:

$$\frac{2m\alpha^2}{\hbar^2} = \frac{2\hbar^2}{\frac{1}{4\pi\epsilon_0} me^4} = \frac{1}{|E_1|}. \quad (3.46)$$

where E_1 is the absolute value of the ground state of energy spectrum from the hydrogen atom: $E_n = -\frac{E_1}{n^2}$. Where it is well known that $E_1 = 13.6eV$. So that (3.45) can be written as:

$$\nabla_{\vec{\eta}}^2 \psi + \frac{2m\alpha^2}{\hbar^2} \left[\epsilon - \frac{qU(\hat{\eta})}{|E_1|} \right] \psi = 0, \quad (3.47)$$

where $\epsilon = \frac{E}{|E_1|}$ is the energy measured in Rydbergs, and the potential is

$$U(\vec{\eta}) \equiv \frac{qU(\vec{r})}{|E_1|} = \frac{q}{|E_1|} \left\{ \frac{1}{4\pi\epsilon_0} \frac{Q}{r} + \frac{1}{4\pi\epsilon_0} \frac{p \cos(\theta)}{r^2} + Ae^{-\left(\frac{r}{\sigma}\right)^2} \right\}. \quad (3.48)$$

To study the possible capture of an electron by the nanoparticle, we take: $q = -e$. We make $Q = Ze$ where Z is the excess number of protons due to the ionization of the nanostructure. So, the first term of (3.48) is

$$U_1(\eta) = \frac{q}{|E_1|} \frac{1}{4\pi\epsilon_0} \frac{Q}{r} = -\frac{2Z}{\eta}. \quad (3.49)$$

The second term is

$$U_2(\eta) = \frac{q}{|E_1|} \frac{1}{4\pi\epsilon_0} \frac{p \cos(\theta)}{r^2} = \frac{2p \cos(\theta)}{a_0 e \eta^2}. \quad (3.50)$$

The unit for the dipole at atomic scales is the Debye: $1 \text{ Debye} = 3.33564 \times 10^{-30} \text{ Cm}$. If p is the electric dipole measured in Debyes $\tilde{D} = \frac{1 \text{ Debye}}{3.33564 \times 10^{-30} \text{ Cm}}$, so that $\tilde{D} = p \times (3.33564 \times 10^{-30} \text{ Cm})$. The factor multiplying the $\cos(\theta)$ is $\frac{2\tilde{D}}{a_0 e} = p \times (0.78686)$. If we denote $g = 0.78686$, it results:

$$U_2(\vec{\eta}) = g \frac{p \cos(\theta)}{\eta^2}.$$

For the third term we take $\sigma = a_0 \sigma_\eta$ and define $\tilde{A} = \frac{eA}{|E_1|}$, so that the height of the Gaussian function will be expressed in Rydbergs from now on.

It results that:

$$U_3(\eta) = \frac{eA}{|E_1|} e^{-\left(\frac{r}{\sigma}\right)^2} = \tilde{A} \exp\left(-\frac{\eta^2}{\sigma_\eta^2}\right). \quad (3.51)$$

In short, we can write the potential as follows:

$$U(\vec{\eta}) = -\frac{2Z}{\eta} + g \frac{p \cos(\theta)}{\eta^2} + \tilde{A} \exp\left(-\frac{\eta^2}{\sigma_\eta^2}\right), \quad (3.52)$$

so the Schrödinger equation is:

$$\nabla_{\vec{\eta}}^2 \psi + \{\epsilon - U(\vec{\eta})\} \psi = 0. \quad (3.53)$$

3.3.2 Separation of variables

The potential $U(\vec{\eta})$ can be written as the sum of a central potential plus another one containing the dipole term. It is defined as:

$$U_\eta = -\frac{2Z}{\eta} + \tilde{A} \exp\left(-\frac{\eta^2}{\sigma_\eta^2}\right), \quad U_\theta = gp \cos(\theta) \quad (3.54)$$

We denote $\nabla_\eta^2 = \frac{\partial^2}{\partial \eta^2} + \frac{1}{\eta} \frac{\partial}{\partial \eta}$ and $\nabla_\theta^2 = \frac{\partial^2}{\partial \theta^2}$, to write the Schrödinger equation as:

$$\left[\nabla_\eta^2 + \frac{1}{\eta^2} \nabla_\theta^2 \right] \psi + \left\{ \epsilon - U_\eta - \frac{1}{\eta^2} U_\theta \right\} \psi = 0 \quad (3.55)$$

We propose a solution of the form $\psi(\eta, \theta, \phi) = R(\eta)F(\theta, \phi)$ where $F(\theta, \phi) = \Theta(\theta)\Phi(\phi)$. The standard way produces three equations. For the radial coordinate it is

$$\nabla_{\eta}^2 R(\eta) + [\epsilon - U_{\eta}] = \lambda R(\eta), \quad (3.56)$$

and for the angular part it is

$$(\nabla_{\Omega}^2 + \lambda - U_{\theta}) F(\theta, \phi) = 0, \quad (3.57)$$

where

$$\nabla_{\Omega}^2 = \hat{D}_{\theta} + \frac{1}{\sin^2(\theta)} \hat{D}_{\phi}, \quad (3.58)$$

with

$$\hat{D}_{\theta} = \frac{1}{\sin(\theta)} \frac{\partial}{\partial \theta} \left(\sin(\theta) \frac{\partial}{\partial \theta} \right), \quad \hat{D}_{\phi} = \frac{\partial^2}{\partial \phi^2}. \quad (3.59)$$

Defining the operator

$$\hat{\beta}_{\Omega} = \hat{D}_{\theta} + \frac{1}{\sin^2(\theta)} \hat{D}_{\phi} + gp \cos(\theta) \quad (3.60)$$

One can directly demonstrate that $[\hat{H}, \hat{\beta}_{\Omega}] = 0$, so that expression (3.60) is analogous to the constant of motion (3.25).

Written in the international system of units, equation (3.57) is the following eigenvalue equation:

$$\hat{\beta}_{\Omega} F(\theta, \phi) = \hbar^2 \lambda F(\theta, \phi), \quad (3.61)$$

where the operator is given by (3.43). So that

$$\hat{\beta}_{\Omega} = -\hbar^2 \left(\hat{D}_{\theta} + \frac{1}{\sin^2(\theta)} \hat{D}_{\phi} \right) + \hbar^2 gp \cos(\theta), \quad (3.62)$$

which is the constant of motion as given by the quantum number λ .

The radial equation can be taken to the form of a one-dimensional Schrödinger equation. We propose $R(\eta) = \frac{u(\eta)}{\eta}$ and obtain

$$\frac{d^2 R_n^{\lambda}}{d\eta^2} + [\epsilon - U_{eff}(\eta)] R_n^{\lambda}(\eta) = 0, \quad (3.63)$$

with effective potential

$$U_{eff}(\eta) = -\frac{2Z}{\eta} + \tilde{A} \exp\left(-\frac{\eta^2}{\sigma_{\eta}^2}\right) + \frac{\lambda}{\eta^2}. \quad (3.64)$$

The quantum number n accounts for the nodes present in the solution of the radial equation. The eigenvalue λ appears in the centrifugal potential and plays a similar role akin to that of an angular momentum. Therefore, we will only consider values for when $\lambda > 0$, due to the fact that for $\lambda < 0$, when the effective potential increases its depth and begins to behave as an anti-centrifugal potential. This is physically unacceptable because in the limit $p \rightarrow 0$, the potential must decrease in depth. This coincides with the results of the classical study of the system where stable orbits are obtained if $\beta > 0$.

Consequently, we have three quantum numbers available to classify the physical states of the system. The angular part of the problem provides two of them: λ and m . The radial part provides the last quantum number, which counts the nodes of the radial function $R_n^\lambda(\eta)$.

The solution is defined in terms of the set of eigenfunctions as follows:

$$\psi_{n,\lambda,m} = R_n^\lambda(\eta)\Theta_\lambda^m(x)\Phi(\phi) \quad (3.65)$$

3.3.3 Angular equation

The equation (3.57) is:

$$\left(\frac{1}{\sin^2(\theta)} \frac{\partial^2}{\partial \phi^2} + \frac{1}{\sin(\theta)} \frac{\partial (\sin(\theta) \frac{\partial}{\partial \theta})}{\partial \theta} + \lambda - U_\theta \right) F(\theta, \phi) = 0. \quad (3.66)$$

The separation constants m^2 and λ are used to obtain the following equations:

$$\frac{d^2\Phi(\phi)}{d\phi^2} + m^2\Phi(\phi) = 0, \quad (3.67)$$

$$(1-x^2)\frac{d^2\Theta(x)}{dx^2} - 2x\frac{d\Theta(x)}{dx} + \left(\lambda - \frac{m^2}{1-x^2} - gpx \right) \Theta(x) = 0, \quad (3.68)$$

where m must be an integer.

We introduce the single-value condition $\Phi(\phi) = \Phi(\phi + 2\pi)$.

Defining the operator

$$\hat{L} = (1-x^2)\frac{d^2}{dx^2} - 2x\frac{d}{dx} - \frac{m^2}{1-x^2}. \quad (3.69)$$

The angular equation is rewritten in the following way:

$$\hat{L}\Theta_\lambda(x) - gpx\Theta_\lambda(x) = -\lambda\Theta_\lambda(x), \quad (3.70)$$

where we find that it is possible to use the property

$$\hat{L}|l, m\rangle = l(l+1)|l, m\rangle, \quad (3.71)$$

where $|l, m\rangle$ are normalized spherical harmonics:

$$|l, m\rangle = Y_l^m(x) = \sqrt{\frac{(2l+1)(l-m)!}{4\pi(l+m)!}} P_l^m(x) e^{im\phi}, \quad (3.72)$$

which fulfill the orthonormalization relations: $\langle l', m' | l, m \rangle = \delta_{l',l} \delta_{m',m}$. We propose building a solution using the expression

$$\Theta_\lambda(x) = \sum_{l=m}^{\infty} C_{ml}^\lambda |l, m\rangle. \quad (3.73)$$

Plugging (3.73) in equation (3.68), one obtains the following matrix equation:

$$\sum_{l=m}^{\infty} C_{ml}^\lambda M_{l,l'} = 0, \quad (3.74)$$

with

$$M_{l,\nu} = [\lambda - l(l+1)] \delta_{\nu,l} - gpN_{\nu,l}, \quad (3.75)$$

and

$$N_{l,\nu} = \langle l', m' | x | l, m \rangle. \quad (3.76)$$

To evaluate (3.76), one can make use of the relations:

$$Y_l^m = \sqrt{\frac{(2l+1)(l-m)!}{4\pi(l+m)!}} P_l^m(x) e^{im\phi}, \quad xP_l^m(x) = \left[\frac{l-m+1}{2l+1} P_{l+1}^m(x) + \frac{l+m}{2l+1} P_{l-1}^m(x) \right],$$

$$Y_{l+1}^m = \sqrt{\frac{(2l+3)(l+1-m)!}{4\pi((l-1+m)!)}} P_l^m(x) e^{im\phi},$$

$$Y_{l-1}^m = \sqrt{\frac{(2l-1)(l-1-m)!}{4\pi((l-1+m)!)}} P_{l-1}^m(x) e^{im\phi}.$$

The result is:

$$xY_l^m = A(l, m)Y_{l+1}^m + B(l, m)Y_{l-1}^m,$$

where

$$A(l, m) = \sqrt{\frac{(l-m+1)(l+m+1)}{(2l+1)(2l+3)}}, \quad B(l, m) = \sqrt{\frac{(l-m)(l+m)}{(2l+1)(2l-1)}}. \quad (3.77)$$

The matrix is of the form

$$N_{\nu,l} = -gp [A(l, m)\delta_{\nu,l+1} + A(l, m)\delta_{\nu,l-1}]. \quad (3.78)$$

Equation (3.74) represents the eigenvalue problem as provided by the quantum number λ , which is associated with the constant of motion $\hat{\beta}_\Omega$, given by (3.43).

As we will see, λ plays role analogous to that of the angular momentum in central field problems and also controls the magnitude of the centrifugal part of the potential.

The solution for the angular part is denoted as

$$F_\lambda^m(\theta, \phi) = \Theta_\lambda^m(x) e^{im\phi} = \sum_{l=m}^{\infty} C_{ml}^\lambda |l, m\rangle e^{im\phi}. \quad (3.79)$$

For every value of m , we have an expression like the one given in (3.73), and the influence of the electric dipole moment is communicated through the matrix in equation (3.78), which provides the elements of the diagonal in $M_{l,\nu}$.

To show its use we will choose several nanostructures with a known electric dipole. One of these could be a small cluster that does not have a spherical shape, however, we establish a working hypothesis where the electron orbitals surrounding the nucleus approach the nanostructure, in such a way that we are allowed to use the expressions given by (3.37-3.38) for the Laplacian as an acceptable approximation.

For every value of p we obtain at least one value for m , which will allow us to calculate the eigenvalues λ and the coefficients $C_{m,l}^\lambda$. We, in turn, calculate the wave function via equation (3.73), which, fortunately, converges quickly so that no more than six terms are needed in order to obtain precision superior to 1×10^{-6} .

$m = 0$

p	$l = 0$	$l = 1$	$l = 2$	$l = 3$	$l = 4$
	$l(l+1) = 0$	$l(l+1) = 2$	$l(l+1) = 6$	$l(l+1) = 12$	$l(l+1) = 20$
p	λ	λ	λ	λ	λ
1	–	2.05822	6.01483	12.0069	20.0040
2	–	2.1987	6.06026	12.0276	20.0161
3	–	2.36089	6.13856	12.0623	20.0362
4	–	2.50135	6.25165	12.1113	20.0645
5	–	2.59682	6.39907	12.1750	20.1010

$m = 1$ (negative values excluded)

p	$l = 0$	$l = 1$	$l = 2$	$l = 3$	$l = 4$
	$l(l+1) = 0$	$l(l+1) = 2$	$l(l+1) = 6$	$l(l+1) = 12$	$l(l+1) = 20$
p	λ	λ	λ	λ	λ
1	0	1.96917	6.00724	12.0069	20.0040
2	0	1.87817	6.02753	12.0276	20.0161
3	0	1.73107	6.05690	12.0623	20.0362
4	0	1.53354	6.08990	12.1113	20.0645
5	0	1.29184	6.12069	12.1750	20.1010

Table 3.1: Eigenvalues λ for $m = 0$, $m = 1$. Electric dipole moments from $p = 1$ to $p = 5$. Comparison with the values $l(l+1)$. Changes grow with p .

3.3.4 Solution to the matrix equation

Equation (3.74) was solved using the software Mathematica to work with finite matrices varying in dimensions of 10 by 10, up to 15 by 15, and finding there is no alteration in the digits of the calculated results. It was also solved using the programming language JULIA and the same results were obtained. We chose the interval $0 \leq p \leq 5$ because this is the range where most of the molecular dipole moments are found. There are clusters that reach higher dipole momenta but they will be explored as special cases later on.

Table 3.1 presents the values of λ for a given p , when $m = 0$ and $m = 1$. The value for $l(l+1)$ is presented in the second row. It is the case for when no dipole is present.

We find that the differences between λ and $l(l+1)$ are very small, meaning that it is not so different from that of the angular part of motion in a central field.

3.3.5 Plots

The physical system can be a sufficiently large cluster of water molecules, or other system of interest. In order to choose the values for the dipole moment we select a nanostructure formed by three molecules of gallium arsenide. As has been reported by Karaminis et. al. [26], the clusters of $(GaAs)_n$ were $n = 3, 4, 5$, show great variety in the ways that they can arrange themselves atomically with different values of electric dipole moment. In particular when $n = 3$, the atomic arrangement has C_s symmetry, where they find that $p = 0.2589$ Debyes. In this case $qgp = 0.814872$ and the eigenvalue $a = 4\lambda$. When the nanostructures are too small the spherical nature of the potential $V_g(\vec{r})$, as seen in (3.33), remains in question, but it is useful to propose this model as a work hypothesis. The eigenvalues are denoted by the symbol

$${}^p\lambda_j^m,$$

where p is the selected dipole moment, m the projection of the angular momentum in the z direction, and j is the increasing order in which the non-negative eigenvalues appear. We only report cases for $m = 0$.

We have analyzed the eigenfunctions of a $(GaAs)_3$ cluster and the most relevant ones are presented in Figure 3.1.

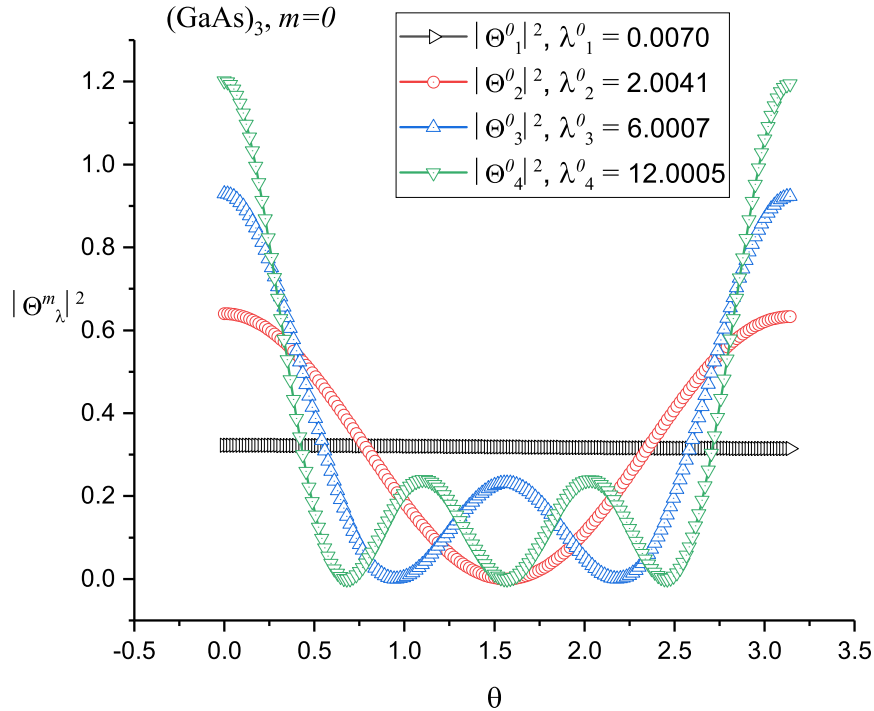


Figure 3.1: Angular probability densities for $(GaAs)_3$, $p = 0.2589$. The values of λ are small modifications of $l(l + 1)$, with $l = 0, 1, 2, 3$. The curves are slightly larger for $\theta \sim 0$.

In order to properly understand the effect of the electric dipole acting on the angular momentum, we compare the eigenfunctions for $(GaAs)_3$, LiC_{60} and RbC_{60} , whose dipoles are $p = \{0.2589, 12.4, 20.6\}$, respectively [2], as seen in Figure 3.2.

When the dipole moment is small, the state Θ_1^0 differs very little from $|0, 1\rangle$ of a central field system; nevertheless, when p grows, we see an increase in probability density towards the hemisphere defined by the inequality $0 \leq \theta \leq \frac{\pi}{2}$. The same thing happens for states Θ_2^0 , Θ_3^0 , Θ_4^0 . This result is to be expected due to the fact that we are describing a negative charge that shows preference towards the direction $\theta = 0$, where the positive part of the dipole is located.

3.4 Radial equation

This section concerns the solution of the radial part for some relevant cases. We take the height \tilde{A} of the Gaussian potential at $10 Ry$, which means it needs an electron with a higher energy than $136 eV$ to cross through the electronic cloud representing the cluster. The width of the Gaussian is chosen in such a way that the potential goes from positive to negative near the $9.44 Bohr$ mark which is approximately 5 \AA . We solve equation (3.63) with a potential given by (3.64) using the shooting method.

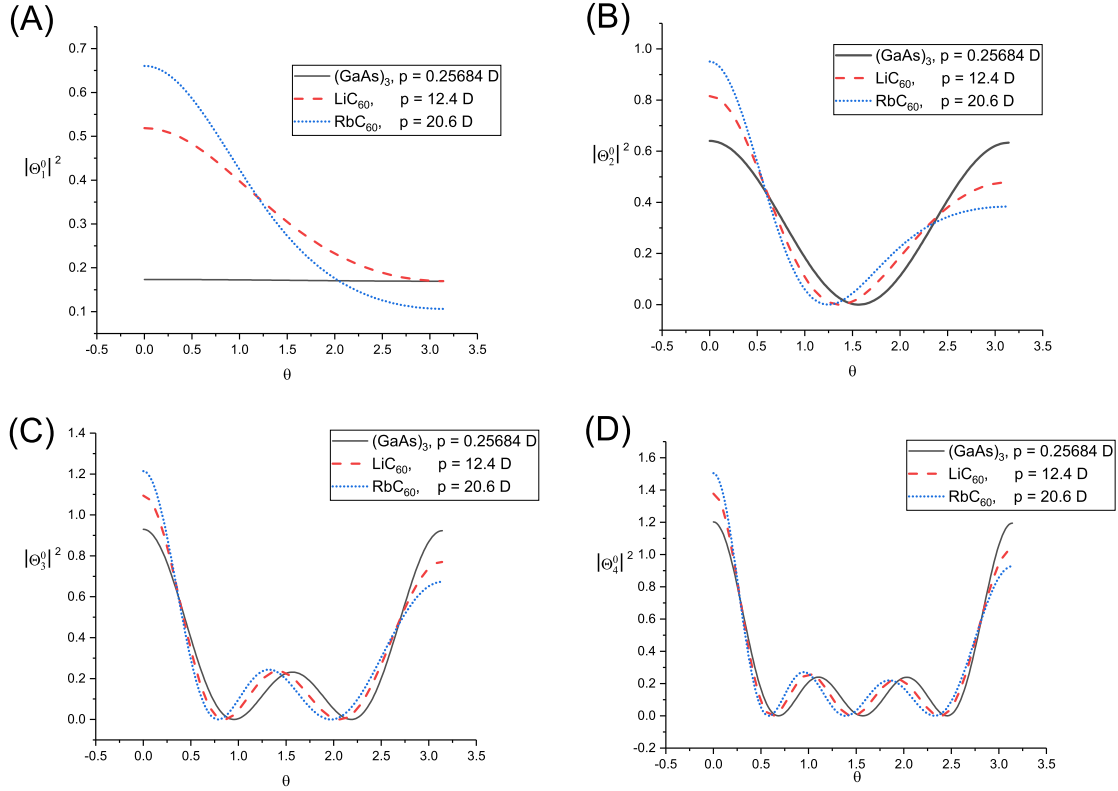


Figure 3.2: Angular probability densities for $(GaAs)_3$, RbC_{60} , and LiC_{60} . When p grows larger, there is a shift in probability towards the lower values of θ .

This allows us to obtain the ground state and up to two excited states. We take the smallest positive eigenvalue for $m = 0$ and set the electric dipole moment to $p = 1$ and $p = 5$. To distinguish between the resulting eigenvalues they are denoted as ${}^p\lambda_j^m$, where p is the value of the dipole moment, m is the projection of the angular momentum in the z axis, and $j = 1, 2$ being the ordering of λ counting from smallest to largest, when p and m have given values.

For $p = 1$, the smallest value ${}^1\lambda_1^0 = 2.05822$. Taking $\sigma = 4.74$, and making calculations produces the eigenfunctions shown in Figure 3.3.

For $p = 5$, we have ${}^5\lambda_0^1 = 2.59682$, and taking $\sigma = 4.72$, as seen in Figure 3.4. Their energies are presented in Table 3.2, where it is clear that the eigenfunctions do not change much and that the values for the energy are very close in spite of the dipole term being multiplied by 5. Thus, we compare the ground states for extremal cases, meaning we take the values ranging from ${}^5\lambda_0^1$ to ${}^5\lambda_0^3$, where the ground states are shown in Figure 3.5.

We observe that when the electric dipole grows, the resultant eigenfunctions slide positively in η but the effect is very slight. This concludes the comparisons of states for the ground state $p = 1$ and $p = 5$. It should be noted that the reach of the interaction between the electron and the cluster is remarkable.

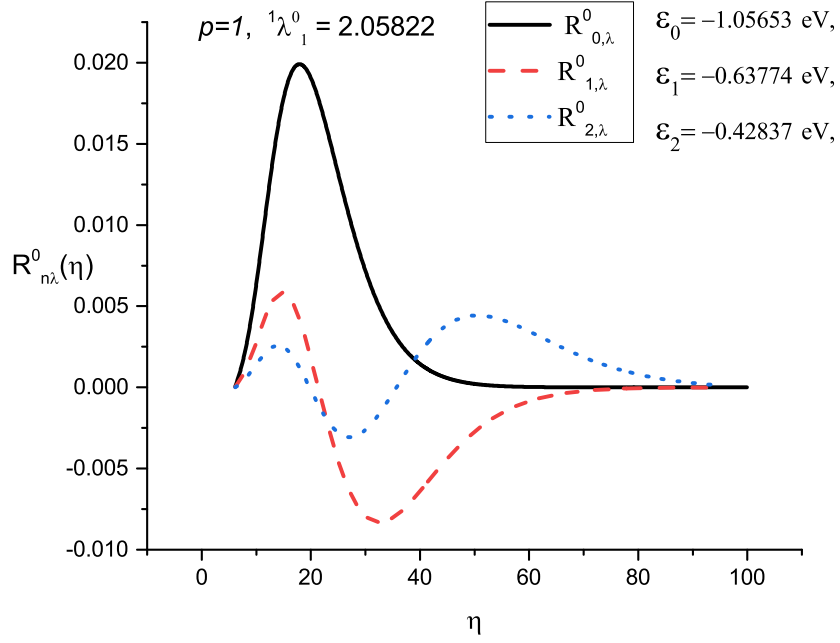


Figure 3.3: Radial probability amplitude for the case when $p = 1$, $\lambda = 2.05822$, $m = 0$, $n = 0, 1, 2$ nodes. The third excited state presents a high probability near 2.6 nm.

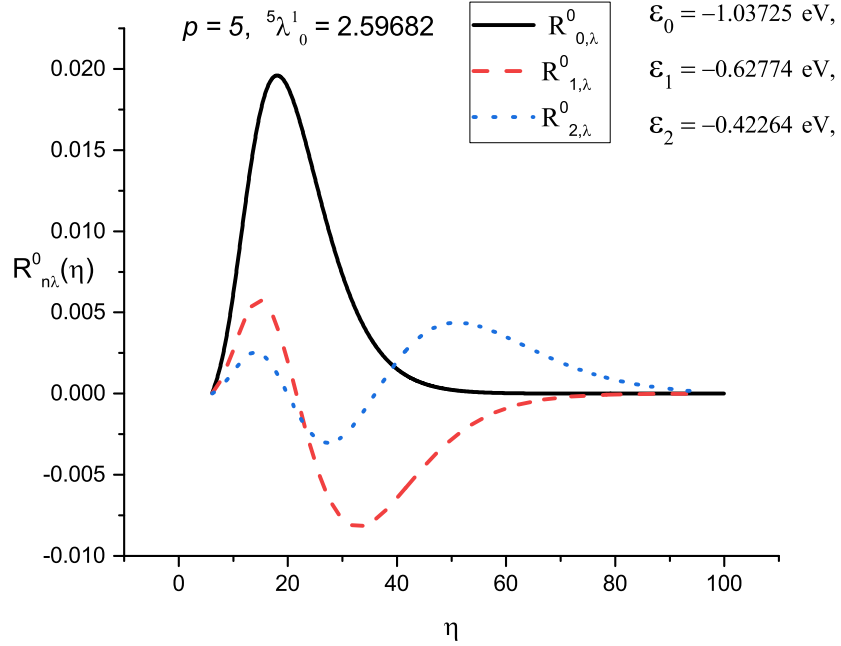


Figure 3.4: Radial probability amplitudes. Case for when $p = 5$, ${}^5\lambda_0^1 = 2.59682$, $m = 0$, $n = 0, 1, 2$ nodes. The energy levels increase slightly and probabilities shift towards the right.

${}^1\lambda_0^1 = 2.05822 \text{ eV}$	${}^5\lambda_0^1 = 2.59682 \text{ eV}$
$\epsilon_0 = -1.05653 \text{ eV}$	$\epsilon_0 = -1.03725 \text{ eV}$
$\epsilon_1 = -0.63774 \text{ eV}$	$\epsilon_1 = -0.62774 \text{ eV}$
$\epsilon_2 = -0.42837 \text{ eV}$	$\epsilon_2 = -0.42264 \text{ eV}$

Table 3.2: Energies for $p = 1$ and $p = 5$. When the eigenvalue λ grows, the energies increase.

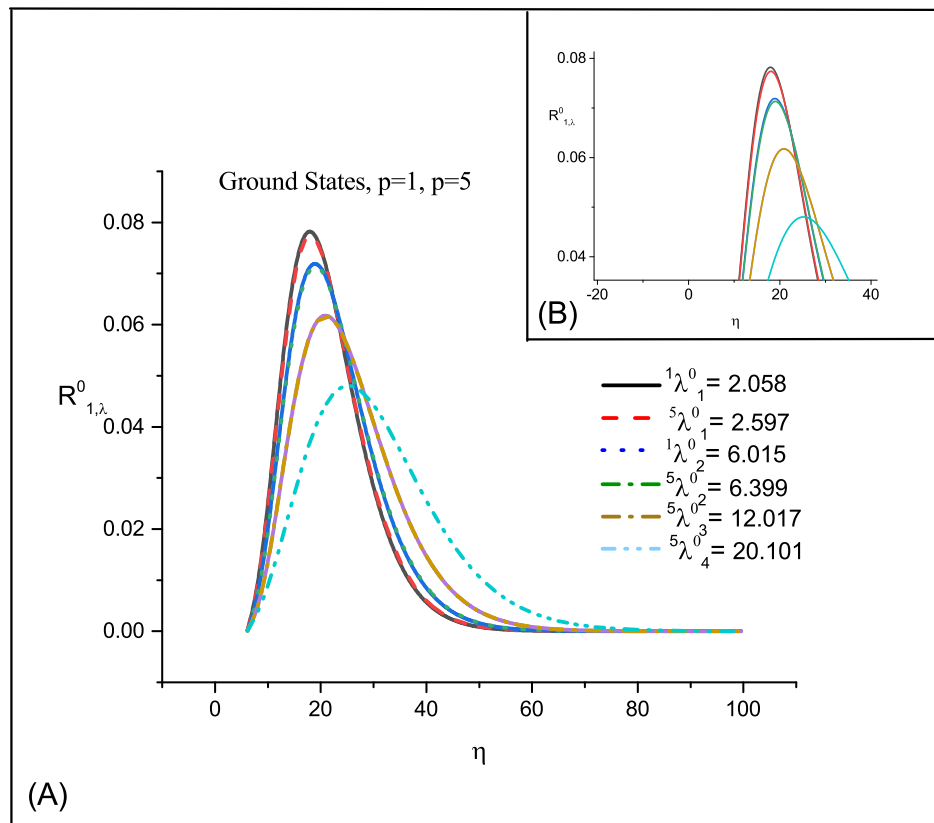


Figure 3.5: A) Radial probability amplitudes for their respective λ with $p = 1$ and $p = 5$. When the values of λ are closer, the curves are barely distinguishable; when it increases, the maximum value of the function decreases and shifts towards the right. B) Enlarging the picture shows the closeness of the curves for similar values of λ .

3.4.1 Ionization energies of the system

In this section, we present the energies of the physical systems that form when a cluster of ionized atoms manages the capture of an electron. It will be shown that they can lose it due to the presence of waves in the infrared spectrum, which makes it possible to detect their presence by looking at the absorption spectra in a controlled experiment. Systems whose electric dipole moments are within the range $1 \leq p \leq 5$ were analyzed. Due to the slow rate of change of energies we report only those with the three non-negative eigenvalues for the case of $p = 1$, and the energies for the fourth non-negative eigenvalue for the case of $p = 5$.

In Table 3.3, at $T = 300$ Kelvin, the excited state ${}^5\lambda_4^0$ has an energy below the numerical value of $K_B T$, where k_B is the Boltzmann constant. In this case, the random collisions coming from the surrounding space can extract the electron, meaning that it is not a stable bound state.

${}^1\lambda_1^0$	absorbed spectral line
-1.05653 eV	1.17346 μm
-0.637741 eV	1.94405 μm
-0.428372 eV	2.89421 μm
${}^1\lambda_2^0$	
-0.918625 eV	1.34963 μm
-0.567026 eV	2.1865 μm
-0.387708 eV	3.19777 μm
${}^1\lambda_3^0$	
-0.734947 eV	1.68693 μm
-0.474507 eV	2.61282 μm
-0.333267 eV	3.72014 μm
${}^5\lambda_4^0$	
-0.540813 eV	2.29247 μm
-0.165757 eV	7.47964 μm
-0.0288181 eV	43.0216 μm

Table 3.3: The electron in any of these energies can absorb infrared radiation to be expelled.

3.5 Conclusions

In this chapter, we have studied the behavior of an electron in the vicinity of a ionized nanoparticle with electric dipole moment. Its presence is modeled using a Gaussian potential whose width can be selected according to the approximate extension of the nanostructure. We demonstrate that there is a constant of motion for these types of non-spherical potentials. It was obtained classically, and we also calculated its quantum operator analogue.

The classical description allows us to show that there are bound orbits in this kind of system.

For the quantum description we have three operators that commute with each other, which means they share eigenfunctions. These are classified using three quantum numbers, one for each operator.

The solution of the angular part of the Schrödinger equation (for the variable θ) differs from the one of the central field only by a single term. We propose using spherical harmonics and find that it converges quickly. We analyzed the angular part of three different systems: $(GaAs)_3$, with a small dipole moment; LiC_{60} , and RbC_{60} , whose electric dipoles are very large. In the first case, the eigenfunctions differ very little from the spherical harmonics, whereas when the electric dipole grows considerably, we can appreciate a shift of the probability density towards $\theta = 0$. This result is to be expected given that electrons tends to move towards the positive region of the dipole.

The radial equation is solved using the shooting method, which allows us to obtain the ground state and the two first excited states with relative ease. In this case, we used the values of $p = 1, 5$ Debyes, to distinguish the effect over the energies and the wave functions. We found that the energy levels shift in the order of 1×10 eV and above, which constitutes a modification of 0.6% to 1.8% with respect to the energy value for $p = 1$ Debyes.

The radial functions also shift their maxima and minima to the right, similar to the case of a small centrifugal effect.

The ground state found for $p = 1$ Debye is 40 times larger than the thermal energy at $T = 300$ K. This means that the bound electron cannot be easily pulled by the thermal noise of a gas. However, it can be forced away by applying electromagnetic energy in the far infrared spectrum. The states described in this chapter can be detected in this manner. The maximum local values that the probability densities can reach, suggest that physical states play an active role in nucleation processes.

BIBLIOGRAPHY

- [1] G Anido and DJ Miller. Electron diffraction by macroscopic objects. *American Journal of Physics*, 52(1):49–54, 1984.
- [2] R Antoine, D Rayane, E Benichou, Ph Dugourd, and M Broyer. Electric dipole moment and charge transfer in alkali-c molecules. *The European Physical Journal D-Atomic, Molecular, Optical and Plasma Physics*, 12(1):147–151, 2000.
- [3] Markus Arndt, Olaf Nairz, Julian Vos-Andreae, Claudia Keller, Gerbrand Van der Zouw, and Anton Zeilinger. Wave–particle duality of c 60 molecules. *nature*, 401(6754):680–682, 1999.
- [4] Herman Batelaan, Eric Jones, Wayne Cheng-Wei Huang, and Roger Bach. Momentum exchange in the electron double-slit experiment. In *J. Phys. Conf. Series*, volume 701, pages 10–1088, 2016.
- [5] Jeff Bezanson, Stefan Karpinski, Viral B Shah, and Alan Edelman. Julia: A fast dynamic language for technical computing. *arXiv preprint arXiv:1209.5145*, 2012.
- [6] Max Born and Emil Wolf. *Principles of optics: electromagnetic theory of propagation, interference and diffraction of light*. Elsevier, 2013.
- [7] Olivier Carnal and Jürgen Mlynek. Young’s double-slit experiment with atoms: A simple atom interferometer. *Physical review letters*, 66(21):2689, 1991.
- [8] Alejandro Castellanos-Jaramillo and Arnulfo Castellanos-Moreno. Spatial and temporal description of electron diffraction through a double slit at the nanometer scale. *European Journal of Physics*, 39(6):065403, 2018.
- [9] Alejandro Castellanos-Jaramillo and Arnulfo Castellanos-Moreno. Bidimensional bound states for charged polar nanoparticles. *Journal of Nanoparticle Research*, 21(7):141, 2019.
- [10] Alejandro Castellanos-Jaramillo, Sergio Gutiérrez-López, and Arnulfo Castellanos-Moreno. Behavior of an electron in the vicinity of a tridimensional charged polar nanoparticle through a classical and quantum constant of motion. *Journal of Nanoparticle Research*, 22(7):1–13, 2020.
- [11] C Cohen-Tannoudji, B Diu, and F Laloe. Quantum mechanics, vol. 1, 231, 2005.

- [12] Roberto Coisson, Graziano Vernizzi, and Xiaoke Yang. Mathieu functions and numerical solutions of the mathieu equation. In *Open-source Software for Scientific Computation (OSSC), 2009 IEEE International Workshop on*, pages 3–10. IEEE, 2009.
- [13] Kevin Connolly and David J Griffiths. Critical dipoles in one, two, and three dimensions. *American Journal of Physics*, 75(6):524–531, 2007.
- [14] Sidney A Coon and Barry R Holstein. Anomalies in quantum mechanics: the $1/r^2$ potential. *American Journal of Physics*, 70(5):513–519, 2002.
- [15] Oakley H Crawford. Bound states of a charged particle in a dipole field. *Proceedings of the Physical Society*, 91(2):279, 1967.
- [16] Clinton Davisson and Lester H Germer. Diffraction of electrons by a crystal of nickel. *Physical review*, 30(6):705, 1927.
- [17] Louis De Broglie. The wave nature of the electron. *Nobel lecture*, 12:244–256, 1929.
- [18] Francisco M Fernández. Bound states of a charged particle in the field of an electric quadrupole in two dimensions. *Journal of Mathematical Chemistry*, 52(6):1576–1580, 2014.
- [19] Kenneth Fox. Simple approximate eigenfunctions for an electron in a finite dipole field. *Physical Review A*, 3(1):13, 1971.
- [20] Richard K Gehrenbeck. Electron diffraction: fifty years ago. *Physics today*, 31(1):34–41, 1978.
- [21] Michel Gondran and Alexandre Gondran. Numerical simulation of the double slit interference with ultracold atoms. *American journal of physics*, 73(6):507–515, 2005.
- [22] Sergio Gutiérrez-López, Arnulfo Castellanos-Moreno, and Rodrigo Arturo Rosas-Burgos. A new constant of motion for an electric charge acted on by a point electric dipole. *American Journal of Physics*, 76(12):1141–1145, 2008.
- [23] Robert Herman and Richard F Wallis. Energy levels of an electron in the field of a finite electric dipole in a magnetic field. *Physical Review B*, 23(10):4902, 1981.
- [24] John D Hunter. Matplotlib: A 2d graphics environment. *Computing in science & engineering*, 9(3):90–95, 2007.
- [25] Eric Jones, Maria Becker, Jom Luiten, and Herman Batelaan. Laser control of electron matter waves. *Laser & Photonics Reviews*, 10(2):214–229, 2016.
- [26] Panagiotis Karamanis, Claude Pouchan, and George Maroulis. Structure, stability, dipole polarizability and differential polarizability in small gallium arsenide clusters from all-electron ab initio and density-functional-theory calculations. *Physical Review A*, 77(1):013201, 2008.

- [27] GA Kerimov and Alberto Ventura. Group-theoretical approach to a non-central extension of the kepler–coulomb problem. *Journal of Physics A: Mathematical and Theoretical*, 43(25):255304, 2010.
- [28] Masashi Kitajima, Takaya Kishino, Takuma Okumura, Naomasa Kobayashi, Atsushi Sayama, Yuma Mori, Kouichi Hosaka, Takeshi Odagiri, Masamitsu Hoshino, and Hiroshi Tanaka. Low-energy and very-low energy total cross sections for electron collisions with n 2. *The European Physical Journal D*, 71(6):139, 2017.
- [29] Hal G Kraus. Huygens–fresnel–kirchhoff wave-front diffraction formulation: paraxial and exact gaussian laser beams. *JOSA A*, 7(1):47–65, 1990.
- [30] JR Nagel. A review and application of the finite-difference time-domain algorithm applied to the schrodinger equation. *ACES Journal-Applied Computational Electromagnetics Society*, 24(1):1, 2009.
- [31] Olaf Nairz, Björn Brezger, Markus Arndt, and Anton Zeilinger. Diffraction of complex molecules by structures made of light. *Physical Review Letters*, 87(16):160401, 2001.
- [32] Carl R Schultheisz. Numerical solution of the huygens–fresnel–kirchhoff diffraction of spherical waves by a circular aperture. *JOSA A*, 11(2):774–778, 1994.
- [33] Fujio Shimizu, Kazuko Shimizu, and Hiroshi Takuma. Double-slit interference with ultracold metastable neon atoms. *Physical Review A*, 46(1):R17, 1992.
- [34] Antonio Soriano, Enrique A Navarro, Jorge A Portı, and Vicente Such. Analysis of the finite difference time domain technique to solve the schrödinger equation for quantum devices. *Journal of Applied Physics*, 95(12):8011–8018, 2004.
- [35] Dennis Sullivan and DS Citrin. Time-domain simulation of two electrons in a quantum dot. *Journal of Applied Physics*, 89(7):3841–3846, 2001.
- [36] Dennis M Sullivan and DS Citrin. Determination of the eigenfunctions of arbitrary nanostructures using time domain simulation. *Journal of applied physics*, 91(5):3219–3226, 2002.
- [37] Dennis M Sullivan and DS Citrin. Time-domain simulation of quantum spin. *Journal of applied physics*, 94(10):6518–6524, 2003.
- [38] Dennis M Sullivan and DS Citrin. Time-domain simulation of a universal quantum gate. *Journal of applied physics*, 96(3):1540–1546, 2004.
- [39] Ffmpeg Team. A complete, cross-platform solution to record, convert, and stream audio and video, 2010.
- [40] James Edward Turner, VE Anderson, and Kenneth Fox. Ground-state energy eigenvalues and eigenfunctions for an electron in an electric-dipole field. *Physical Review*, 174(1):81, 1968.
- [41] Ramses Van Zon. Effective pair potentials for spherical nanoparticles. *Journal of statistical mechanics: theory and experiment*, 2009(02):P02008, 2009.

- [42] Richard F Wallis, Robert Herman, and Harold Willis Milnes. Energy levels of an electron in the field of a finite dipole. *Journal of Molecular Spectroscopy*, 4(1-6):51–74, 1960.
- [43] Xiang-Yao Wu, Bai-Jun Zhang, Xiao-Jing Liu, Bing Liu, Chun-Li Zhang, and Jing-Wu Li. Quantum theory of neutron diffraction. *International Journal of Modern Physics B*, 23(15):3255–3264, 2009.
- [44] Xiaoyan YZ Xiong and WEI Sha. The fdtd method: Essences, evolutions, and applications to nano-optics and quantum physics. *Computational Nanotechnology Using Finite Difference Time Domain*, 2:37–82, 2013.
- [45] Hirofumi Yanagisawa, Marcelo Ciappina, Christian Hafner, Johannes Schötz, Jürg Osterwalder, and Matthias F Kling. Optical control of young’s type double-slit interferometer for laser-induced electron emission from a nano-tip. *Scientific reports*, 7(1):1–9, 2017.
- [46] Kane Yee. Numerical solution of initial boundary value problems involving maxwell’s equations in isotropic media. *IEEE Transactions on antennas and propagation*, 14(3):302–307, 1966.
- [47] Anton Zeilinger, Roland Gähler, CG Shull, Wolfgang Treimer, and Walter Mampe. Single-and double-slit diffraction of neutrons. *Reviews of modern physics*, 60(4):1067, 1988.